Cell Reports

Article

# GABAergic-like dopamine synapses in the brain

## Graphical abstract

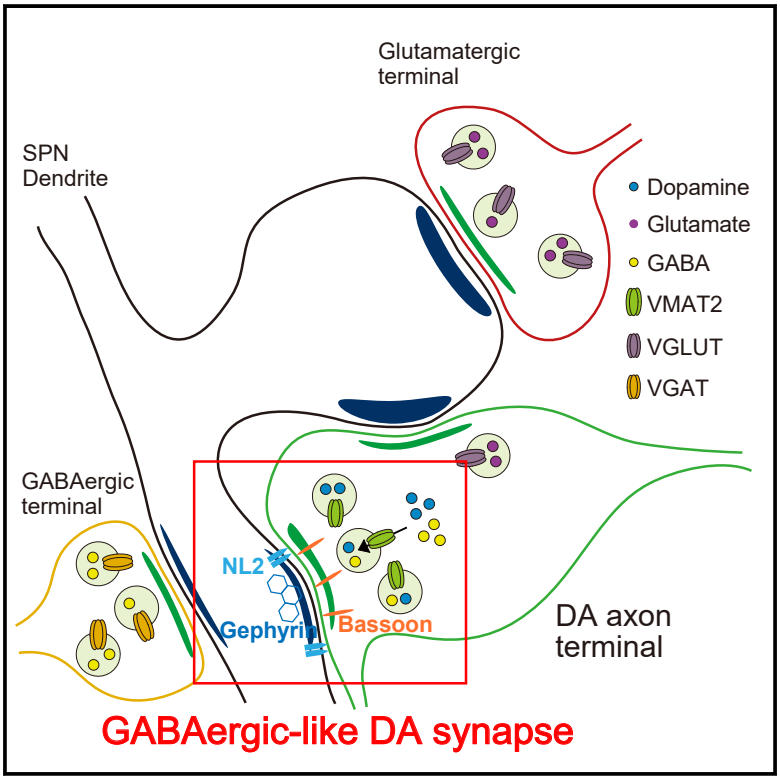


## Authors

Hyun-Jin Kim, Byungjae Hwang, Maria Reva, ..., Ja-Hyun Baik, Jung-Hoon Park, Jae-Ick Kim

## Correspondence

jikim220@unist.ac.kr

## In brief

Kim et al. discover that GABAergic-like dopamine synapses exist in the brain. GABA co-transmission at these synapses can be critical for the survival and maintenance of dopamine synapses in health and brain diseases.

## Highlights

- GABAergic-like DA synapses exist in the brain with regional heterogeneity
- GABA co-transmission is physiologically distinct from typical GABA transmission
- GABA co-transmission can be critical for the maintenance of DA synapses
- GABA co-transmission attenuates faster than DA transmission in animal models of PD

Kim et al., 2023, Cell Reports *42*, 113239
October 31, 2023 
https://doi.org/10.1016/j.celrep.2023.113239

CellPress

Cell Reports

CellPress
OPEN ACCESS

Article

# GABAergic-like dopamine synapses in the brain

Hyun-Jin Kim,[1] Byungjae Hwang,[2,9] Maria Reva,[3,4,8,9] Jieun Lee,[1] Byeong Eun Lee,[1] Youngeun Lee,[1] Eun Jeong Cho,[1] Minseok Jeong,[1] Seung Eun Lee,[5] Kyungjae Myung,[2,6] Ja-Hyun Baik,[7] Jung-Hoon Park,[2] and Jae-Ick Kim[1,10,*]

[1]Department of Biological Sciences, Ulsan National Institute of Science and Technology (UNIST), Ulsan 44919, Republic of Korea
[2]Department of Biomedical Engineering, Ulsan National Institute of Science and Technology (UNIST), Ulsan 44919, Republic of Korea
[3]Institut Pasteur, Unit of Synapse and Circuit Dynamics, CNRS UMR, 3571 Paris, France
[4]Sorbonne University, ED3C, Paris, France
[5]Research Animal Resource Center, Korea Institute of Science and Technology (KIST), Seoul 02792, Republic of Korea
[6]Center for Genomic Integrity, Institute for Basic Science (IBS), Ulsan 44919, Republic of Korea
[7]Department of Life Sciences, Korea University, Seoul 02841, Republic of Korea
[8]Present address: Blue Brain Project (BBP), École Polytechnique Fédérale de Lausanne (EPFL), Campus Biotech, 1202 Geneva, Switzerland
[9]These authors contributed equally
[10]Lead contact
*Correspondence: jikim220@unist.ac.kr
https://doi.org/10.1016/j.celrep.2023.113239

## SUMMARY

Dopamine synapses play a crucial role in volitional movement and reward-related behaviors, while dysfunction of dopamine synapses causes various psychiatric and neurological disorders. Despite this significance, the true biological nature of dopamine synapses remains poorly understood. Here, we show that dopamine transmission is strongly correlated with GABA co-transmission across the brain and dopamine synapses are structured and function like GABAergic synapses with marked regional heterogeneity. In addition, GABAergic-like dopamine synapses are clustered on the dendrites, and GABA transmission at dopamine synapses has distinct physiological properties. Interestingly, the knockdown of neuroligin-2, a key postsynaptic protein at GABAergic synapses, unexpectedly does not weaken GABA co-transmission but instead facilitates it at dopamine synapses in the striatal neurons. More importantly, the attenuation of GABA co-transmission precedes deficits in dopaminergic transmission in animal models of Parkinson's disease. Our findings reveal the spatial and functional nature of GABAergic-like dopamine synapses in health and disease.

## INTRODUCTION

Dopamine (DA) orchestrates essential brain functions including voluntary movement, action selection, and reward-related behaviors via volume transmission.[1,2] Due to its spatiotemporal release properties, synaptic transmission through DA synapses has been considered slow and diffuse in space, possibly causing non-synapse-specific transfer of information to postsynaptic neurons. In addition, DA acts through extrasynaptic G protein-coupled receptors.[3,4] Thus, the early idea that DA transmission is slow, inaccurate, and non-synapse specific has been prevalent for a long time. However, recent studies highlighted the possibility that synaptic action via DA synapses can be rapid, synapse specific, and far more complicated than we think. It appears that there exist active zone-like release sites in some populations of DA boutons that can potentially support spatially and temporally precise coding.[5] More interestingly, co-transmission of classical, fast-acting neurotransmitters such as glutamate and γ-aminobutyric acid (GABA) at DA synapses has been found in the striatum.[6–8] Given that DA release and its propagation to neighboring synapses via volume transmission are not strictly limited in space, such co-transmission of fast-acting neurotransmitters at DA synapses and its synaptic effects would be spatially more restricted and probably localized to individual synapses, rendering the physiological actions of DA synapses more synapse specific. Although potentially critical for realistic synaptic actions at DA synapses, the central question of whether this co-transmission of DA, glutamate, and GABA at DA synapses is ubiquitous throughout the brain or is just one of the distinctive features of some specific DA projections remains not fully explored.

In this study, we designated DA synapses as GABAergic-like DA synapses where dopaminergic presynaptic boutons capable of co-transmitting GABA are closely apposed to GABAergic postsynaptic sites. GABA co-transmission at these DA synapses is presumed to have essential functions in regulating neural circuits.[9] To gain insights into the possible functions of GABA co-transmission at DA synapses in the brain, we investigated spatial and physiological features of GABAergic-like DA synapses.

## RESULTS

### GABA co-transmission co-exists with DA transmission at DA synapses in the brain

To determine brain-wide heterogeneity of synaptic actions at DA synapses caused by the co-transmission of multiple

neurotransmitters, we first revisited regional variations of DA axons by labeling tyrosine hydroxylase (TH) and dopamine transporter (DAT), which are key molecular markers for DA neurons and axons. Two DA axonal projections (nigrostriatal and mesocorticolimbic) from DA neurons in the substantia nigra pars compacta (SNc) and ventral tegmental area heavily innervate striatum,[10] which is the input region of basal ganglia (Figure 1A). However, they also project to the cortex and other nuclei of basal ganglia, including globus pallidus and subthalamic nucleus.[11] Most of the striatal areas were occupied by highly dense arborization of DA axons (Figures 1A and 1B) and the areas of TH-positive axons were comparable among striatal regions (Figures 1B and 1C). The amount of axonal projections to the cortex, however, was significantly less than DA projections in the striatum. Extrastriatal basal ganglia nuclei showed much sparser axonal fibers than the striatum, but TH-positive DA axons in these regions were still denser than other cortical areas (Figures 1B, 1C, and 1E). The regional pattern of DAT-positive axons was largely similar to the one of TH-positive axons except in cortical regions, where less consistency was found between TH- and DAT-positive axons (Figures 1B, 1D, and 1F). Notably, although small, regional heterogeneity and differences were found within the striatum in DAT-positive axons.

We next questioned whether neurotransmitter co-transmission at DA synapses would follow the quantitative pattern of axons across the brain. We selectively expressed channelrhodopsin 2 (ChR2) in DA neurons by crossing DAT-IRES-Cre mice with Ai32 mice.[7] The regional expression pattern of ChR2 in DAT-Cre;Ai32 mice was very similar to the ones obtained by TH and DAT immunostaining (Figures S1A–S1C). We performed fast-scanning cyclic voltammetry (FSCV) to compare brain-wide DA transmission (Figure 1G). Similar to the previous reports on electrically stimulated DA transmission,[12,13] light-evoked DA transmission was the highest in the dorsal striatum, and ventral domains of the striatum exhibited relatively smaller DA release than dorsal striatum (Figures 1H–1J and S1D–S1F). Photo-stimulation of DA axons elicited very low DA release in the cortex as well as extrastriatal basal ganglia nuclei.

We then sought to determine the regional heterogeneity in the co-transmission of GABA and glutamate at DA synapses. To measure inhibitory postsynaptic current (IPSC) and excitatory postsynaptic current (EPSC), we performed whole-cell voltage-clamp recording in various postsynaptic neurons of DA target areas and recorded optogenetically induced IPSC (oIPSC) and EPSC (oEPSC) from the same postsynaptic neuron. The strongest GABAergic responses were observed in the dorsal striatum, while the ventral striatum only displayed GABAergic responses less than half of the dorsal striatum. GABA co-transmission at DA synapses in both cortex and extracellular basal ganglia nuclei was minimal (Figures 1K–1M, S1J, S1K, and S1O–S1Q). Unlike GABA co-transmission, the highest responses by glutamatergic co-transmission came from the nucleus accumbens (NAc) shell in the ventral striatum (Figures S1G–S1I, S1L, S1M, and S1O–S1Q). Glutamatergic oEPSCs in other striatal domains were much smaller than that of the NAc shell and there were almost no EPSCs from the cortex and extrastriatal basal ganglia nuclei. The reason behind this marked heterogeneity in the glutamate co-transmission at DA synapses might be a brain region-specific expression of VGlut2 (vesicular glutamate transporter 2) that is essential for DA-glutamate co-transmission at DA synapses. Of particular note, when this regional transmission of DA, GABA, and glutamate at DA synapses was compared with each other, we found a strong correlation between DA and GABA release, whereas no pronounced correlations existed between glutamate and other neurotransmitters (Figure 1N). In addition, when the area of DA axons and neurotransmitters co-transmission were compared, significant correlations were found between DA axonal areas and GABA (or DA) transmission, while there was no correlation between DA fibers and glutamate transmission (Figures 1O and S1N). Interestingly, the correlation between DAT-positive axons and GABA (or DA) transmission was stronger than the one by TH-positive axons. Together, DA transmission reliably accompanies GABA transmission at DA synapses, especially in striatal regions. Furthermore, regional heterogeneity of DAT-positive axons in the brain, although small, mirrors regional differences in DA and GABA transmissions better than TH-positive axons.

## Spatial distribution and characteristics of GABAergic-like DA synapses in the brain

DA axon terminals make synaptic contacts with neurons in numerous brain areas, although the majority of these synapses reside within the striatum. It is important to note that not all TH-positive bouton-like structures can release DA[5] and postsynaptic DA receptors are typically at extrasynaptic sites.[3,4,14] Thus, unlike glutamatergic and GABAergic synapses, this mismatch between presynaptic and postsynaptic sites, and our lack of knowledge about presynaptic and postsynaptic molecular markers defining functional DA synapses, have hampered the comprehensive identification of spatial and functional features of DA synapses throughout the brain. Recently, neuroligin-2 (NL2), a common postsynaptic cell adhesion molecule that has been thought to be exclusively localized to inhibitory synapses,[15] was found in the postsynaptic membrane specializations at striatal DA synapses.[4] Despite this finding, our understanding of molecular components defining DA synapses in the brain is still far from complete.

We investigated the brain-wide distribution and spatial characteristics of DA synapses by labeling molecular markers for both presynaptic and postsynaptic sites. We utilized NL2 as a postsynaptic marker for DA synapse. We also considered the co-localization of TH and vesicular monoamine transporter 2 (VMAT2) immunofluorescences as a putative marker for dopaminergic boutons that can co-transmit DA and GABA.[6] In multi-color immunostaining and airyscan confocal microscopy, TH- and VMAT2-positive presynaptic boutons, unlike TH-positive axons, showed marked regional heterogeneity in their distribution across the nigrostriatal and mesocorticolimbic pathways (Figures 2A–2D). The dorsal striatum largely contained more TH- and VMAT2-positive boutons than the ventral striatum. Notably, the number of NL2-positive postsynaptic sites also exhibited regional differences across the brain (Figure 2C). We then regarded the co-localization of a TH- and VMAT2-positive presynaptic bouton and an NL2-positive postsynaptic site as a potential GABAergic-like DA synapse. When this triple co-localization was compared, the regional heterogeneity in dopaminergic

CellPress
OPEN ACCESS

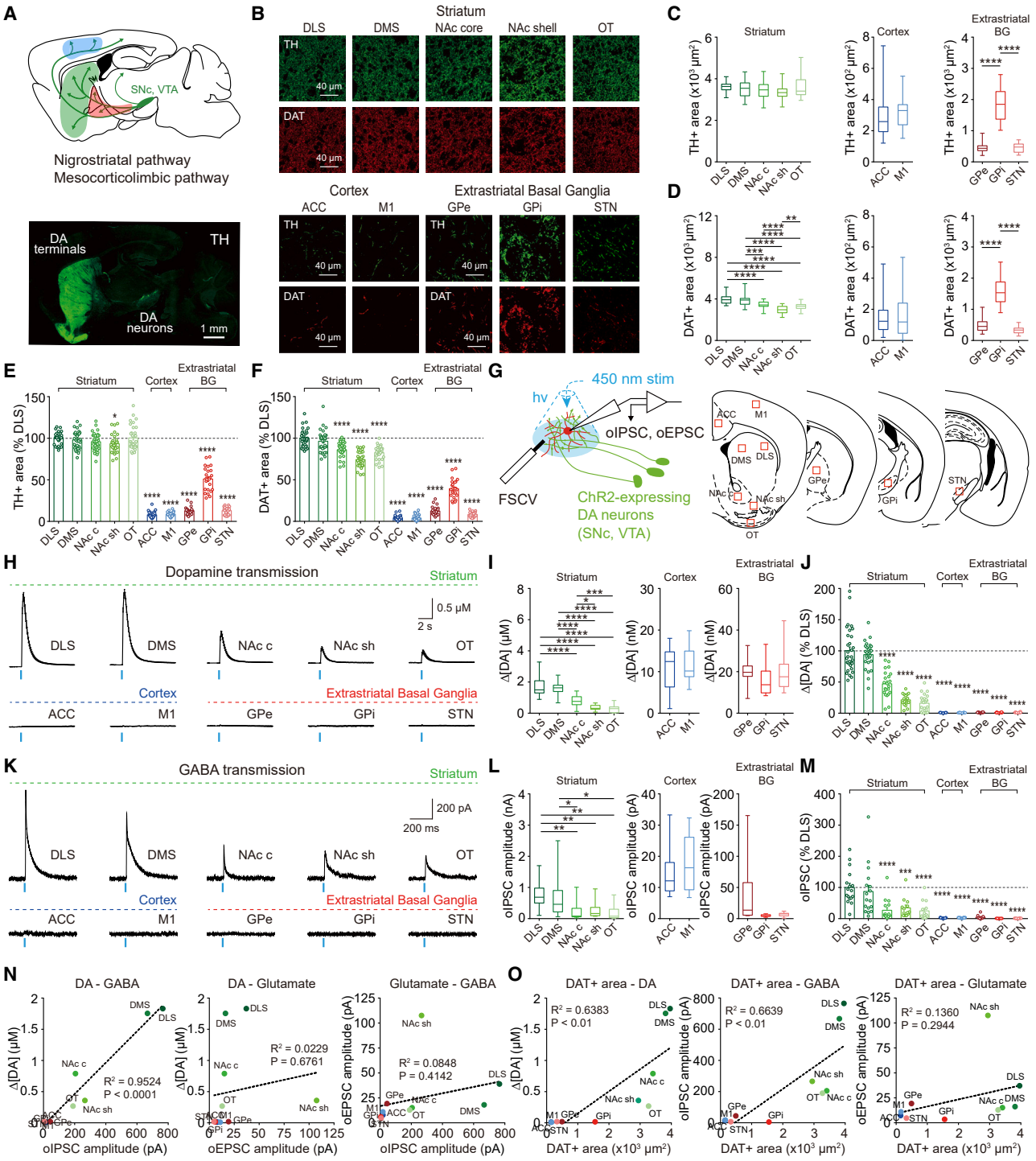


**Figure 1. GABA co-transmission co-exists with DA transmission at DA synapses in the brain**

(A) Schematic illustration and fluorescent image of dopaminergic pathways in the brain.

(B) Representative confocal images of TH+ and DAT+ DA fibers in the brain of DAT-Cre mice.

(C–F) Summary statistics of TH+ and DAT+ axonal areas in the brain (n = 24–34 images).

(G) Schematic illustration depicting electrophysiological recording of synaptic transmission at DA synapses in the multiple brain regions.

(H–J) Representative recording traces and summary statistics of DA transmission in the brain (n = 12–32 slices).

(K–M) Representative recording traces and summary statistics of GABA transmission at DA synapses (n = 7–17 cells).

(N) Relationships between DA, GABA, and glutamate transmission.

(O) Relationships between DAT+ area and neurotransmitters release. The blue bar indicates optogenetic light stimulation. Data are presented as box and whisker plots or mean ± SEM. *p < 0.05, **p < 0.01, ***p < 0.001, ****p < 0.0001. See also Figure S1 and Table S1.

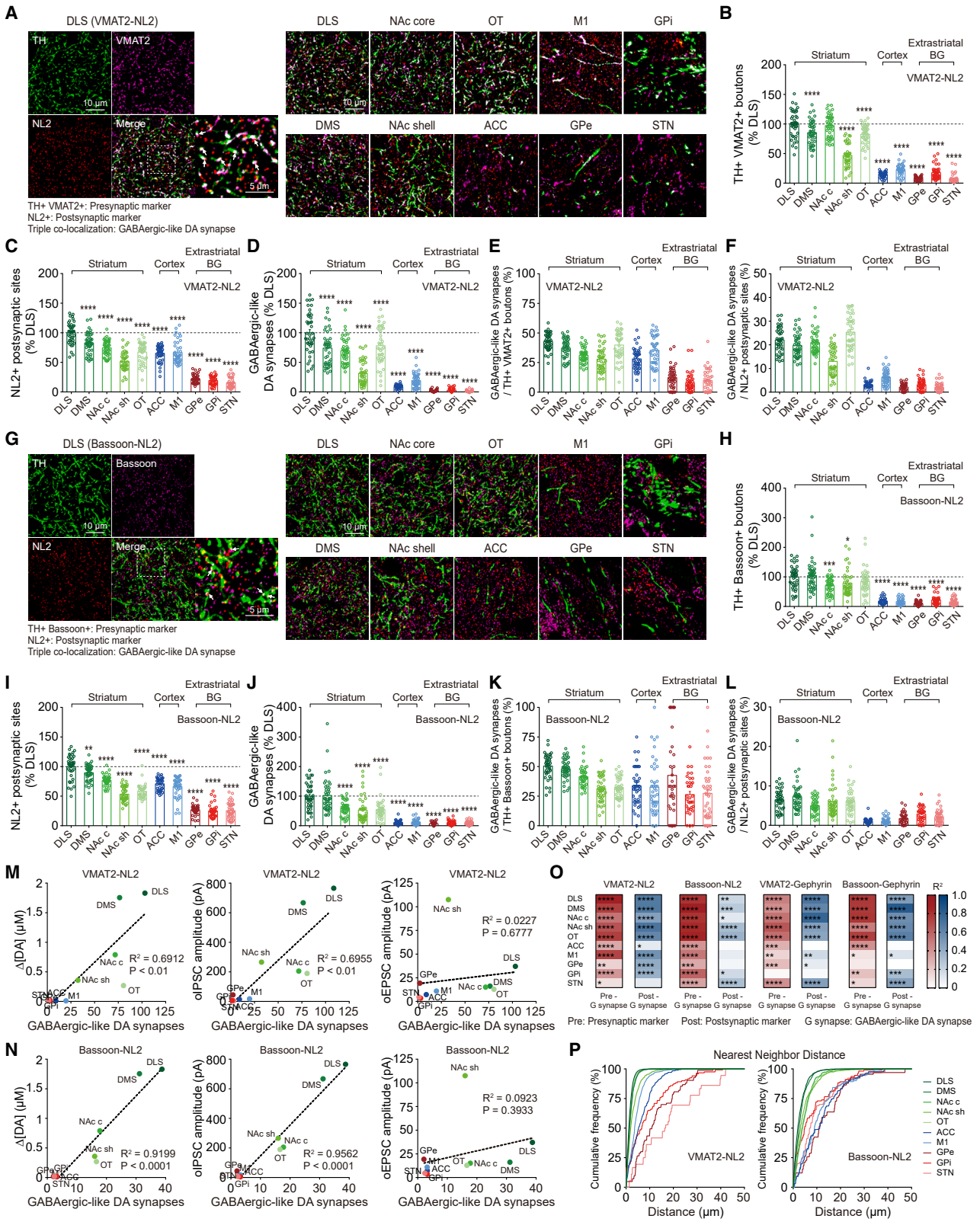


*(legend on next page)*

presynaptic boutons was accentuated by variation in NL2-positive postsynaptic sites, leading to more prominent differences in the number of GABAergic-like DA synapses across the brain (Figure 2D).

It is likely that TH- and VMAT2-positive presynaptic boutons may not represent functional DA terminals capable of releasing neurotransmitters as VMAT2 can also exist outside synaptic boutons. To confirm this, we examined the spatial properties of GABAergic-like DA synapses by labeling the presynaptic protein Bassoon as a functional presynaptic marker at DA synapses. Bassoon is present in presynaptic active zones and has been recently shown to mark functional DA boutons.[5,16] When VMAT2 was replaced by Bassoon, relative regional differences in the numbers of both presynaptic boutons and GABAergic-like DA synapses were largely maintained (Figures 2G–2J), while the estimated numbers of dopaminergic boutons and GABAergic-like DA synapses were considerably reduced. In addition, when Bassoon was used as a presynaptic marker, the difference in the number of GABAergic-like DA synapses among brain regions, especially between the dorsal and ventral striatum, became more pronounced (Figure 2J). To validate whether GABAergic-like DA synapses were properly captured by enhanced confocal microscopy, we performed expansion microscopy, which can visualize the synapses in a higher resolution.[17] The number of GABAergic-like DA synapses measured by airyscan imaging was similar to the number detected by expansion microscopy (Figures S2A–S2C). We also utilized the shuffling analysis to prove that the GABAergic-like DA synapses we identified are not caused by non-specific labeling.[5] The number of GABAergic-like DA synapses was significantly reduced when shuffled NL2 was used in place of actual NL2 (Figures S2D–S2F). These results clearly verify that our imaging method and analysis can properly capture GABAergic-like DA synapses.

We further validated our findings by using Gephyrin as a postsynaptic marker for DA synapses. Gephyrin is an assembly protein that anchors inhibitory neurotransmitter receptors to the postsynaptic membrane and has been determined as a major postsynaptic protein of GABAergic synapses.[18,19] Spatial distribution and regional disparity of GABAergic-like DA synapses, revealed by Gephyrin, were also comparable with the pattern identified by NL2, supporting the distinct regional properties of GABAergic-like DA synapses in the brain. Moreover, compared with the co-localization of VMAT2 and Gephyrin, the identification of GABAergic-like DA synapses by the co-localization of Bassoon and Gephyrin made the regional difference between dorsal and ventral striatum more obvious (Figures S2G–S2R). Noticeably, when Bassoon was used in place of VMAT2 as a presynaptic marker, the proportion of GABAergic-like DA synapses out of all the presynaptic boutons increased, whereas the ratio of GABAergic-like DA synapses out of all the postsynaptic sites significantly decreased (Figures 2E, 2F, 2K, 2L, S2K, S2L, S2Q, and S2R).

We also found that the Bassoon-NL2 combination exhibited the strongest correlation between GABAergic-like DA synapses and dopaminergic boutons and the weakest correlation between GABAergic-like DA synapses and GABAergic postsynaptic sites when the correlations were separately calculated and compared from each brain area (Figure 2O). More importantly, the correlation between GABAergic-like DA synapses and GABA (or DA) transmission was the highest and highly significant in the brain, when both Bassoon and NL2 were simultaneously used as molecular markers for GABAergic-like DA synapses (Figures 2M and 2N). No significant correlations were found between GABAergic-like DA synapses and glutamate transmission. We further performed nearest-neighbor analysis on the distribution of GABAergic-like DA synapses across the brain. Among the different combinations of presynaptic and postsynaptic markers, the Bassoon-NL2 combination showed a clear distinction in the distribution of GABAergic-like DA synapses between the dorsal and ventral striatum (Figure 2P). This Bassoon-NL2 combination also displayed a significant separation of inter-synaptic distances between the striatum and other brain areas. Together, these results indicate that, unlike just the area of DA axons, GABAergic-like DA synapses are distributed throughout the brain with significant regional and spatial heterogeneity, irrespective of synaptic markers used for analysis. Furthermore, GABAergic-like DA synapses determined by Bassoon-NL2 combination correlate best with GABA-DA transmission at DA synapses.

## Spatial clustering of GABAergic-like DA synapses in the striatum

Spatial arrangement and clustering of synapses can exert complex effects on the computation of neural circuits.[20,21] We again used triple co-localization of TH, Bassoon, and NL2 as a marker for GABAergic-like DA synapses. To better capture region-specific spatial clustering of GABAergic-like DA synapses, the image area per each brain region was expanded (Figure S3A). For spatial clustering analysis, we utilized Ripley's H function, which is particularly sensitive to point pattern clustering.[22,23] Owing to the limited number of GABAergic-like DA synapses in other brain areas, we analyzed spatial clustering for only striatal regions that contain the sufficient number of GABAergic-like DA

**Figure 2. Spatial distribution and characteristics of GABAergic-like DA synapses in the brain**

(A) Enhanced confocal (airyscan) images of brain-wide DA axons and synapses immunostained by TH, VMAT2, and NL2 antibodies (white arrow, triple co-localization).

(B–F) Summary statistics of brain-wide GABAergic-like DA synapses (n = 39–42 images). (G) Enhanced confocal images of brain-wide DA axons and synapses immunostained by TH, Bassoon, and NL2 antibodies.

(H–L) Summary statistics of brain-wide GABAergic-like DA synapses (n = 36–42 images).

(M and N) Relationships between GABAergic-like DA synapses and neurotransmitters release at DA synapses.

(O) Relationships between GABAergic-like DA synapses and DA boutons (or GABAergic postsynaptic sites).

(P) Cumulative frequency for nearest neighbor distance among GABAergic-like DA synapses. Data are presented as mean ± SEM. *p < 0.05, **p < 0.01, ***p < 0.001, ****p < 0.0001. See also Figures S2 and S3 and Table S1.

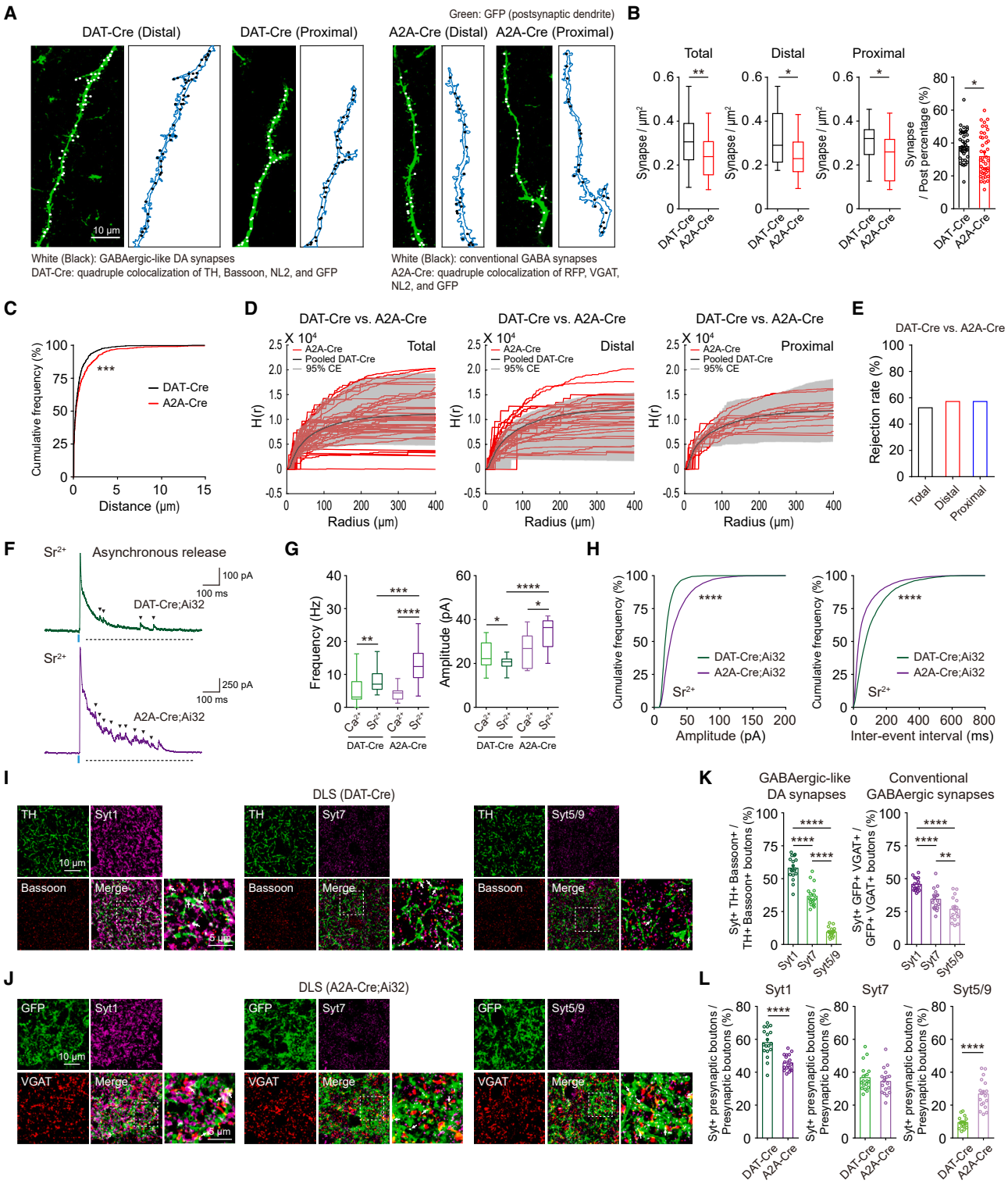


**Figure 3. Physiological differences between GABAergic-like DA synapses and conventional GABAergic synapses in the dorsal striatum**

(A) Enhanced confocal images of GABAergic-like DA (or conventional GABAergic) synapses and sparsely labeled SPN dendrites in the dorsal striatum of DAT-Cre and A2A-Cre mice (only GFP signal and synapses are shown for clarity).

(B) Summary statistics of synapse density on SPN dendrites (n = 14–42 images).

(C) Cumulative frequency of nearest neighbor distance for GABAergic-like DA synapses (DAT-Cre) or GABAergic synapses (A2A-Cre).

*(legend continued on next page)*

synapses to perform Ripley's H function. In the mean nearest neighbor distance, the dorsomedial striatum (DMS) alone showed significantly shorter inter-synaptic distances than the null model (random distribution) (Figure S3B). However, according to Ripley's H function, all the striatal regions exhibited marked differences in the clustering of GABAergic-like DA synapses when compared with the simulated random arrangement of synapses from the null models (Figures S3C and S3D).

To further compare the relative clustering of GABAergic-like DA synapses between striatal regions, we analyzed the same Ripley's H function with one of the striatal regions pooled as a null model. We found that significantly strong differences were observed between the dorsolateral striatum (DLS) and all the striatal regions when DLS was used as the null model (Figures S3E and S3F). Both dorsal and ventral striatum showed more than 60% of rejection rates calculated as the number of samples for which the null model rejected on the Diggle-Cressie-Loosmore-Ford (DCLF) test.[24] Moreover, when the olfactory tubercle (OT) was used as the null model, these regional differences in the clustering of GABAergic-like DA synapses were preserved (Figures S3G and S3H). It is important to note that GABAergic-like DA synapses in the DLS seem to be the most dispersed among the striatal regions even though DLS has the greatest number of GABAergic-like DA synapses. This regional heterogeneity in the clustering of GABAergic-like DA synapses might have functional implications for the regulation of striatal microcircuits.

## Physiological differences between GABAergic-like DA synapses and conventional GABAergic synapses in the dorsal striatum

Functional properties of GABAergic-like DA synapses have not been explored previously in the brain. To address this, we chose striatal collateral inhibition from indirect SPNs (iSPNs) to other SPNs as a case of conventional GABAergic connection and first compared the spatial clustering of GABAergic-like DA synapses and conventional GABAergic synapses in the dorsal striatum. As both DA and local GABAergic inputs form synapses on the dendrites of SPNs, we sparsely labeled SPNs in the dorsal striatum of both DAT-Cre and A2A-Cre mice (in which Cre recombinase is selectively expressed in iSPNs) by expressing green fluorescent protein (GFP) via virus injection. For selectively labeling conventional GABAergic axons from iSPNs to other SPNs, we also injected adeno-associated virus (AAV)-expressing red fluorescent protein (RFP) upon exposure to Cre recombinase into the dorsal striatum of A2A-Cre mice (Figure S4A). Triple co-localization of TH, Bassoon, and NL2 on the GFP-positive postsynaptic dendrite was considered as a GABAergic-like DA synapse, as in Figure 2. In addition, we regarded the triple co-localization of RFP, VGAT (vesicular GABA transporter), and NL2 as a conventional GABAergic synapse (Figure 3A). We found that the density of GABAergic-like DA synapses on the single dendrite of SPNs was markedly higher than that of conventional GABAergic synapses made by local iSPNs. Furthermore, this difference in the density of synapses was maintained irrespective of the specific location on the dendrite (distal vs. proximal) (Figure 3B). Inter-synaptic distances of GABAergic-like DA synapses were also shorter than that of GABAergic synapses (Figure 3C). The spatial clustering of synapses on a single dendrite matters since it can critically affect the functional computation of dendrites.[25,26] Hence, we employed Ripley's H function to characterize the spatial clustering of GABAergic-like DA synapses and GABAergic synapses within a single dendrite. When considering both Ripley's H function analysis and DCLF test, conventional GABAergic synapses made by iSPNs appeared to be more clustered than GABAergic-like DA synapses, only at the distal portion of dendrites (Figures 3D and 3E). Rejection rates of more than 50% from the whole and proximal dendrites in the DCLF test seem to be caused by the fact that the clustering patterns of GABAergic synapses are more variable than that of GABAergic-like DA synapses on the entire and proximal dendrites of SPNs.

To better understand physiological differences between GABAergic-like DA synapses and conventional GABAergic synapses, we first examined whether GABA co-transmission at DA synapses and GABA transmission at conventional GABAergic synapses rely on distinct types of voltage-dependent $Ca^{2+}$ channels for vesicular release. We evaluated the effects of three different types of $Ca^{2+}$ channels blockers on the amplitude of oIPSCs in SPNs. We found that GABA release at DA terminals is dependent on N-type as well as P/Q type $Ca^{2+}$ channels in the dorsal striatum, whereas T-type $Ca^{2+}$ channels were not implicated in vesicular release (Figures S4B, S4D, and S4F). On the other hand, conventional GABAergic transmission, which was examined at GABAergic synapses between iSPN and dSPN, was mediated by not only N- and P/Q-type $Ca^{2+}$ channels but also T-type channel (Figures S4C, S4E, and S4G).

Next, we questioned whether GABA co-transmission and conventional GABA transmission share similar or distinct quantal properties. To compare the quantal properties of oIPSCs in the dorsal striatum, $Ca^{2+}$ was replaced with $Sr^{2+}$ in the bath solution to promote asynchronous release. $Sr^{2+}$ facilitated asynchronous vesicle release in both DAT-Cre;Ai32 and A2A-Cre;Ai32 mice, while GABA co-transmission at DA synapses was less prone to evoke asynchronous release than conventional GABAergic transmission (Figures 3F and 3G). Furthermore, the quantal amplitude of GABA co-transmission was markedly smaller than that of conventional GABA transmission between the SPNs

(D) Edge-corrected Ripley's H function analysis of GABAergic synapses and GABAergic-like DA synapses (null model; CE. confidence envelope).
(E) Rejection rate of conventional GABAergic synapses from GABAergic-like DA synapses (null model) evaluated by DCLF test.
(F–H) Representative recording traces and summary statistics of optogenetically evoked asynchronous GABA release in DAT-Cre;Ai32 and A2A-Cre;Ai32 mice during the bath-application of strontium (black arrowhead, asynchronous release events) (n = 11–30 cells).
(I and J) Enhanced confocal images of synaptotagmins (1, 7, 5/9) immunofluorescence in DAT-Cre and A2A-Cre;Ai32 mice (white arrow, presynaptic boutons co-localized with synaptotagmins).
(K and L) Proportion of DA (or GABAergic) presynaptic boutons co-localized with synaptotagmin 1, 7, and 5/9 (n = 18 images). Data are presented as box and whisker plots or mean ± SEM. *p < 0.05, **p < 0.01, ***p < 0.001, ****p < 0.0001. See also Figure S4 and Table S1.

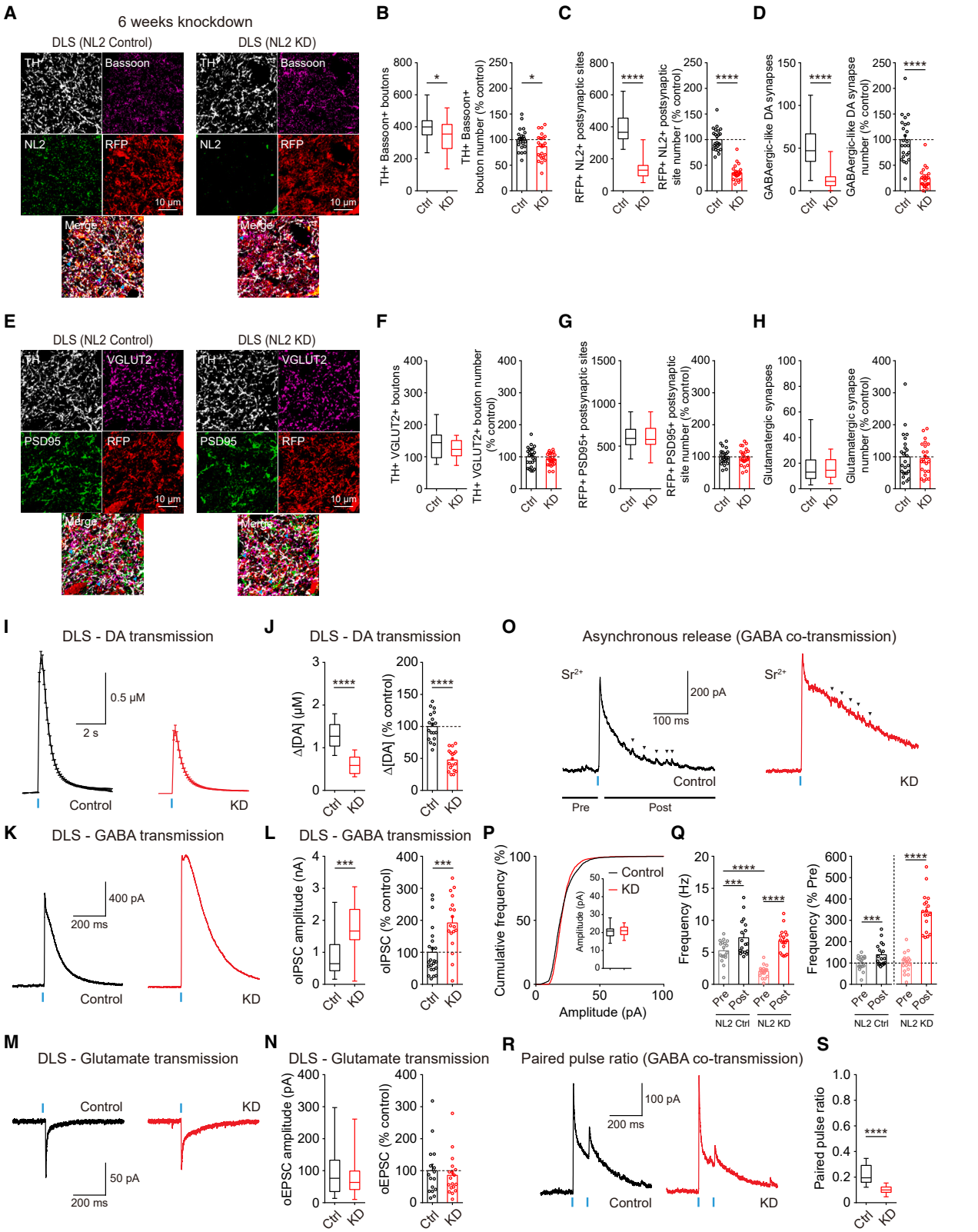


*(legend on next page)*

(Figures 3G and 3H). To validate our quantal analysis at DA synapses, we broadly suppressed the conventional GABAergic transmission to SPNs by virally expressing Gi-coupled designer receptors exclusively activated by designer drugs in the striatum. Although the quantal frequency of GABA co-transmission at DA synapses was slightly decreased possibly due to the inhibition of cholinergic interneurons, we found that the quantal properties of GABA co-transmission in this condition are largely comparable with the ones in Figure 3 (Figures S4H and S4I). These results were further confirmed by another $Sr^{2+}$ experiment in which high chloride internal solution was used (Figures S4J and S4K); a better signal-to-noise ratio is achieved, and clamping conditions are enhanced by high chloride internal solution.[27]

To search for the presynaptic molecular mechanisms behind the differential susceptibility to asynchronous release by $Sr^{2+}$, we checked the individual isoforms of synaptotagmin enriched at DA and GABAergic terminals (Figures 3I and 3J). DA terminals were preferentially co-localized with synaptotagmin 1, followed by synaptotagmin 7 and 5/9 in the dorsal striatum. In addition, the relative expression levels of each synaptotagmin isoform at conventional GABAergic terminals were similar to DA terminals (Figures 3I–3K). However, the co-localization of synaptotagmin 1, which is critical for synchronous vesicular release,[28–30] was considerably higher at DA terminals than at GABAergic terminals (Figure 3L), possibly accounting for the observed differential susceptibility to asynchronous release by $Sr^{2+}$ at DA and GABAergic terminals.

## GABAergic synaptic contact and transmission may be critical for the maintenance of DA synapses

NL2 has been known to be an essential molecule in the formation, maintenance, and function of GABAergic synapses in various brain regions.[31,32] To determine the functional significance of NL2 and GABA co-transmission at DA synapses, we performed knockdown (KD) of NL2 by expressing a shRNA KD virus in striatal neurons for 6 weeks (Figures S5A and S5B). We found that NL2 KD for 6 weeks significantly reduces the numbers of presynaptic DA boutons, NL2-positive postsynaptic sites, and GABAergic-like DA synapses, while the number of TH, VGlut2, and PSD-95 (postsynaptic density protein 95)-positive glutamatergic synaptic contacts was unchanged (Figures 4A–4H). Unlike the recent report using microRNA-based lentivirus for NL2 KD in the striatum of newborn pups,[4] NL2 KD also slightly diminished the number of another GABAergic postsynaptic marker Gephyrin as well as NL2, although the expression level of $GABA_AR\alpha1$ was not altered in striatal neurons (Figures S5C–S5J).

To investigate the physiological consequences of NL2 KD on the synaptic transmission at DA synapses, we first evaluated DA transmission. DA transmission was markedly attenuated by NL2 KD in postsynaptic striatal neurons (Figures 4I and 4J). We also confirmed that glutamate co-transmission is unaffected by NL2 KD (Figures 4M and 4N). Strikingly and unexpectedly, however, NL2 KD in striatal neurons did not decrease but instead significantly increased GABA co-transmission at DA synapses, which is opposite to what was found in DA transmission (Figures 4K and 4L). Given that the number of GABAergic-like DA synapses was reduced by NL2 KD, we hypothesized that GABA co-transmission might be functionally facilitated to compensate for the reduction of GABAergic-like DA synapses. NL2 KD in the striatum of A2A-Cre;Ai32 mice significantly decreased conventional GABA transmission (Figures S6A and S6B), as shown in previous literature.[31–33]

To search for potential mechanisms behind the upregulation of GABA co-transmission, we first checked KD-induced alteration of quantal properties of GABA transmission by examining $Sr^{2+}$-mediated asynchronous synaptic release. We found that NL2 KD in striatal neurons has no effect on the quantal amplitude of GABA co-transmission at DA synapses (Figures 4O and 4P). Spontaneous IPSC frequency was significantly reduced in NL2 KD mice, which was revealed by baseline spontaneous IPSC rate before optogenetic stimulation. Upon light stimulation of DA terminals, however, the frequencies of asynchronous GABA release were comparable between control and NL2 KD mice. Furthermore, the increase of quantal frequency by light stimulation was approximately 6-fold higher in NL2 KD mice than in control mice (Figures 4O–4Q). As reported by the previous study,[34] the rate of occurrence of asynchronous release is correlated with the probability of synchronous evoked release. Thus, our results indicate that, although the number of GABAergic-like DA synapses was markedly reduced by NL2 KD, GABA transmission at DA synapses was not decreased, but rather increased via a presynaptic mechanism.

To confirm our findings, we examined the paired pulse ratio of GABA co-transmission at DA synapses by delivering paired light stimuli and found that the presynaptic release probability of GABA transmission is substantially enhanced by NL2 KD (Figures 4R and 4S). This enhancement in the release probability of GABA co-transmission was corroborated by two additional experiments. In the first experiment, we held the membrane

**Figure 4. NL2 and GABA transmission can be crucial for the maintenance of DA synapses in the dorsal striatum**

(A) Enhanced confocal images of GABAergic-like DA synapses in the dorsal striatum of DAT-Cre mice injected with NL2 control and KD viruses (expressed for 6 weeks) (blue arrowhead, quadruple co-localization).

(B–D) Summary statistics of GABAergic-like DA synapses (n = 24 images).

(E) Enhanced confocal images of glutamatergic synapses.

(F–H) Summary statistics of glutamatergic synapses (n = 24 images).

(I and J) Representative recording traces and summary statistics of DA transmission at DA synapses (n = 18 slices).

(K and L) Representative recording traces and summary statistics of GABA transmission at DA synapses (n = 18–23 cells).

(M and N) Representative recording traces and summary statistics of glutamate transmission at DA synapses (n = 16–18 cells).

(O–Q) Representative recording traces and summary statistics for frequency and amplitude of asynchronous GABA release at DA synapses (black arrowhead, asynchronous release event) (n = 18 cells).

(R and S) Representative recording traces and summary statistics for paired pulse ratio of oIPSC at DA synapses (n = 17 cells). Data are presented as box and whisker plots or mean ± SEM. *p < 0.05, ***p < 0.001, ****p < 0.0001. See also Figures S5 and S6 and Table S1.

potential of patched neurons at −30 mV and used weak light stimulation to mitigate clamping errors. In the second experiment, we utilized ChETA, a channelrhodopsin with faster kinetics than ChR2-H134R. In these experiments, we further proved that the presynaptic release probability of GABA transmission at DA synapses is significantly enhanced by NL2 KD (Figures S6C–S6F). Interestingly, we found that the size of TH- and Bassoon-positive DA boutons that survived from NL2 KD is significantly increased in NL2 KD mice (Figures S5K and S5L). To provide more evidence of the contrasting effects of NL2 KD on DA and GABA transmissions, we took advantage of the mGIRK2 by which DA transmission can be translated into potassium current. By expressing the mGIRK2 in striatal neurons, we could simultaneously monitor both DA transmission and GABA co-transmission from a single postsynaptic iSPN.[35] In this experiment, D2 receptor-mediated IPSCs were diminished, whereas $GABA_A$-mediated IPSCs were markedly facilitated by NL2 KD, verifying our findings in Figure 4 (Figures S6G–S6I).

To further validate our hypothesis, we observed the long-term effects of NL2 KD (12 weeks) on DA synapses. As expected, the number of presynaptic DA boutons, NL2-positive postsynaptic sites, and GABAergic-like DA synapses were all significantly decreased by long-term NL2 KD (Figures 5A–5D). Notably, the long-term KD of NL2 greatly decreased the number of DA boutons compared with short-term KD, indicating that NL2 in striatal neurons is essential for the survival and maintenance of DA synapses. Unlike short-term NL2 KD, the number of glutamatergic contacts at DA synapses was also reduced by long-term NL2 KD (Figures 5E–5H), implying that both glutamatergic and dopaminergic microdomains at DA synapses eventually degenerate in the absence of NL2 in striatal neurons.[36] As we originally hypothesized, the long-term NL2 KD finally weakened GABA co-transmission at DA synapses, and glutamate co-transmission was also diminished (Figures 5I–5N). Our findings collectively suggest that not only NL2 at postsynaptic sites but also GABA co-transmission may be necessary for the maintenance of DA synapses in the striatum.

## The weakening of GABA transmission precedes the deficit of DA transmission at DA synapses in animal models of Parkinson's disease

Physiological changes such as altered neuronal firing in DA neurons and the attenuation of DA transmission have been reported to precede the degeneration of DA neurons in the course of Parkinson's disease (PD).[13,37] We questioned whether the co-transmission of multiple neurotransmitters at DA synapses is equally susceptible to the progression of PD. To unravel the potential deficits of synaptic transmission at DA synapses, we induced the animal model of PD by infusing 6-OHDA (6-hydroxydopamine) unilaterally into the medial forebrain bundle (MFB) of DAT-Cre mice (Figure 6A). We first checked the degeneration of GABAergic-like DA synapses in the dorsal striatum by simultaneously labeling TH, Bassoon, and NL2 (Figure 6B). We found that GABAergic-like DA synapses in the ipsilateral striatum are largely intact 1 day after 6-OHDA injection. However, when compared with the contralateral striatum, GABAergic-like DA synapses began to decrease substantially 3 days after 6-OHDA injection. The number of GABAergic-like DA synapses was significantly reduced 7 days after 6-OHDA injection (Figure 6C). In addition, the spatial distribution of GABAergic-like DA synapses became sparser as 6-OHDA-induced pathology progressed (Figure 6D).

We then examined the time-dependent alteration of DA transmission 1, 3, and 7 days after 6-OHDA injection. To identify DA synapse-specific physiological changes, we unilaterally injected 6-OHDA into the MFB of DAT-Cre;Ai32 mice (Figure 6E). As with the number of GABAergic-like DA synapses over time, DA transmission in the ipsilateral striatum was not affected 1 day after 6-OHDA injection, while the release of DA was dramatically reduced 3 and 7 days after 6-OHDA injection (Figures 6F and 6G). Most interestingly, however, GABA transmission at DA synapses began to significantly diminish even one day after 6-OHDA injection (Figures 6H, 6I, and S7A). Like DA transmission, GABA transmission measured 3 and 7 days after 6-OHDA injection was also considerably weakened when compared with the contralateral striatum. In the case of glutamate transmission at DA synapses, no attenuation of oEPSC was observed 1 day after injection. Since the magnitude of glutamate co-transmission at DA synapses was relatively small when compared with DA or GABA co-transmission, glutamate transmission was almost abolished 3 and 7 days after 6-OHDA injection (Figures 6J, 6K, and S7B). Our results were further supported by an additional experiment using a genetically encodable fluorescent DA sensor dLight1.3b.[38] As in the FSCV experiment, the fluorescent signals that represent DA transmission captured by postsynaptic neurons also began to decrease 3 and 7 days after 6-OHDA injection (Figures S7C and S7D). These results strongly suggest that, although GABA transmission co-exists with DA transmission at DA synapses in the normal brain, DA and GABA transmission may change over the course of PD with differential temporal susceptibility.

It has been reported that alterations of aldehyde dehydrogenase 1a1 (ALDH1a1) in midbrain DA neurons are associated with PD.[39–41] In addition, it was recently shown that ALDH1a1 can synthesize GABA in midbrain DA neurons.[7] Hence, we checked whether the timing of a reduction in ALDH1a1 expression is commensurate with time-dependent attenuation of GABA transmission at DA synapses by 6-OHDA injection. We confirmed that most of TH-positive DA axons also express ALDH1a1 in the dorsal striatum (Figure S7E). Then we found that the expression of ALDH1a1 in the ipsilateral striatum already begins to decrease 1 day after 6-OHDA injection, as in the case of time-dependent attenuation of GABA transmission (Figures 6L and 6M). Notably, the level of TH expression was not affected 1 day after 6-OHDA injection, and the expression of both ALDH1a1 and TH was similarly reduced to a large extent 3 and 7 days after 6-OHDA injection (Figures 6L, 6M, S7F, and S7G).

To further corroborate our findings, we examined another animal model of PD where AAVs expressing a mutated form (A53T) of α-synuclein were injected into the SNc of DAT-Cre and DAT-Cre;Ai32 mice. In this alternative form of the PD mouse model, PD-related pathophysiological changes progress over a longer period of time (Figures 7A and 7D). As in the 6-OHDA-induced PD model, comparable findings were obtained from the α-synuclein-induced PD model, and GABA co-transmission alone started to decrease 2 weeks after AAV injection (Figures 7G

CellPress
OPEN ACCESS

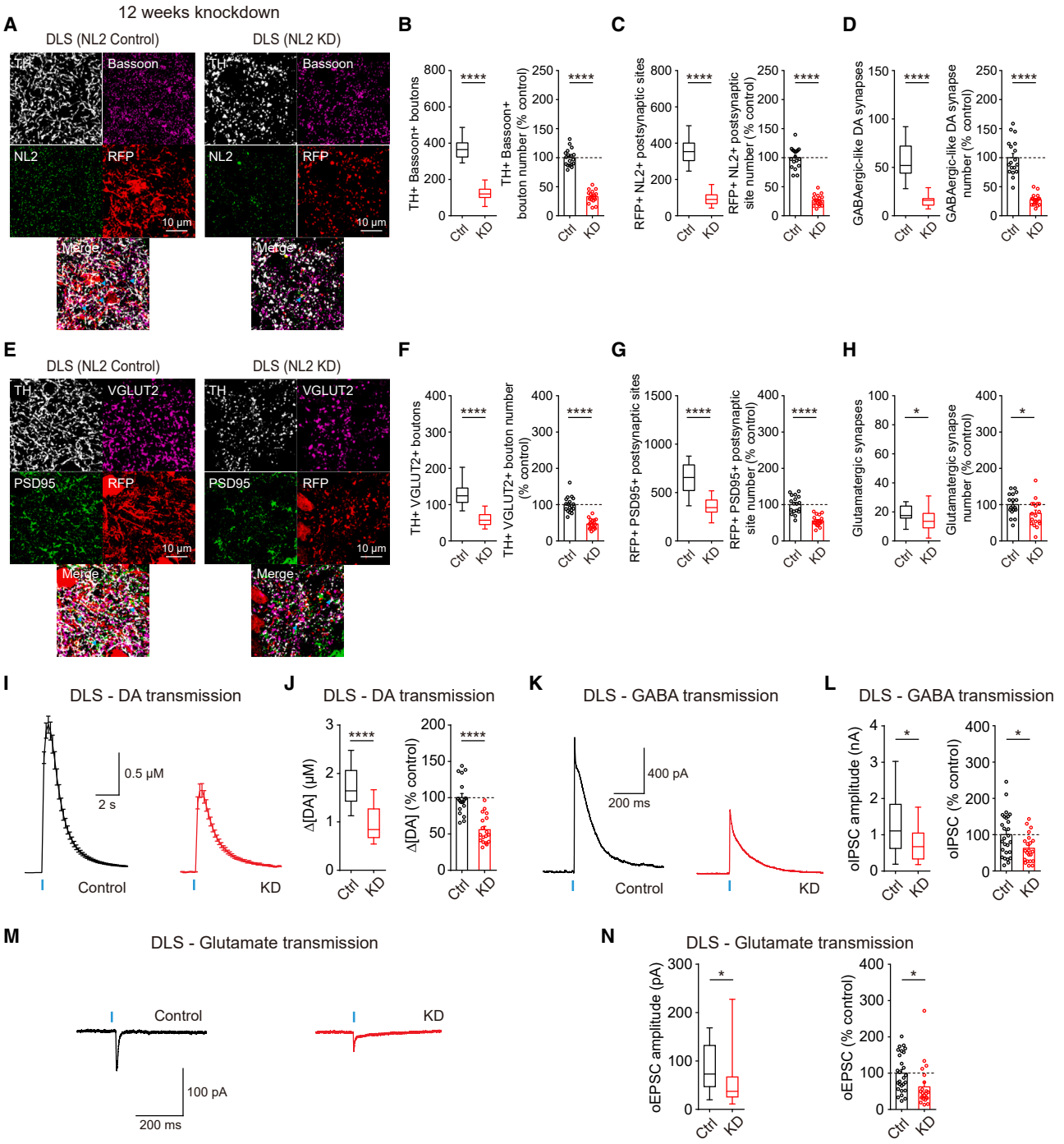


**Figure 5. Long-term depletion of NL2 leads to the downregulation of DA synapses and GABA co-transmission in the dorsal striatum**

(A) Enhanced confocal images of GABAergic-like DA synapses in the dorsal striatum of DAT-Cre mice injected with NL2 control and KD viruses (expressed for 12 weeks) (blue arrowhead, quadruple co-localization).

(B–D) Summary statistics of GABAergic-like DA synapses (n = 18 images).

(E) Enhanced confocal images of glutamatergic synapses.

(F–H) Summary statistics of glutamatergic synapses (n = 18 images).

(I and J) Representative recording traces and summary statistics of DA transmission at DA synapses (n = 18 slices).

(K and L) Representative recording traces and summary statistics of GABA transmission at DA synapses (n = 22–27 cells).

(M and N) Representative recording traces and summary statistics of glutamate transmission at DA synapses (n = 22–27 cells). Data are presented as box and whisker plots or mean ± SEM. *p < 0.05, ****p < 0.0001. See also Table S1.

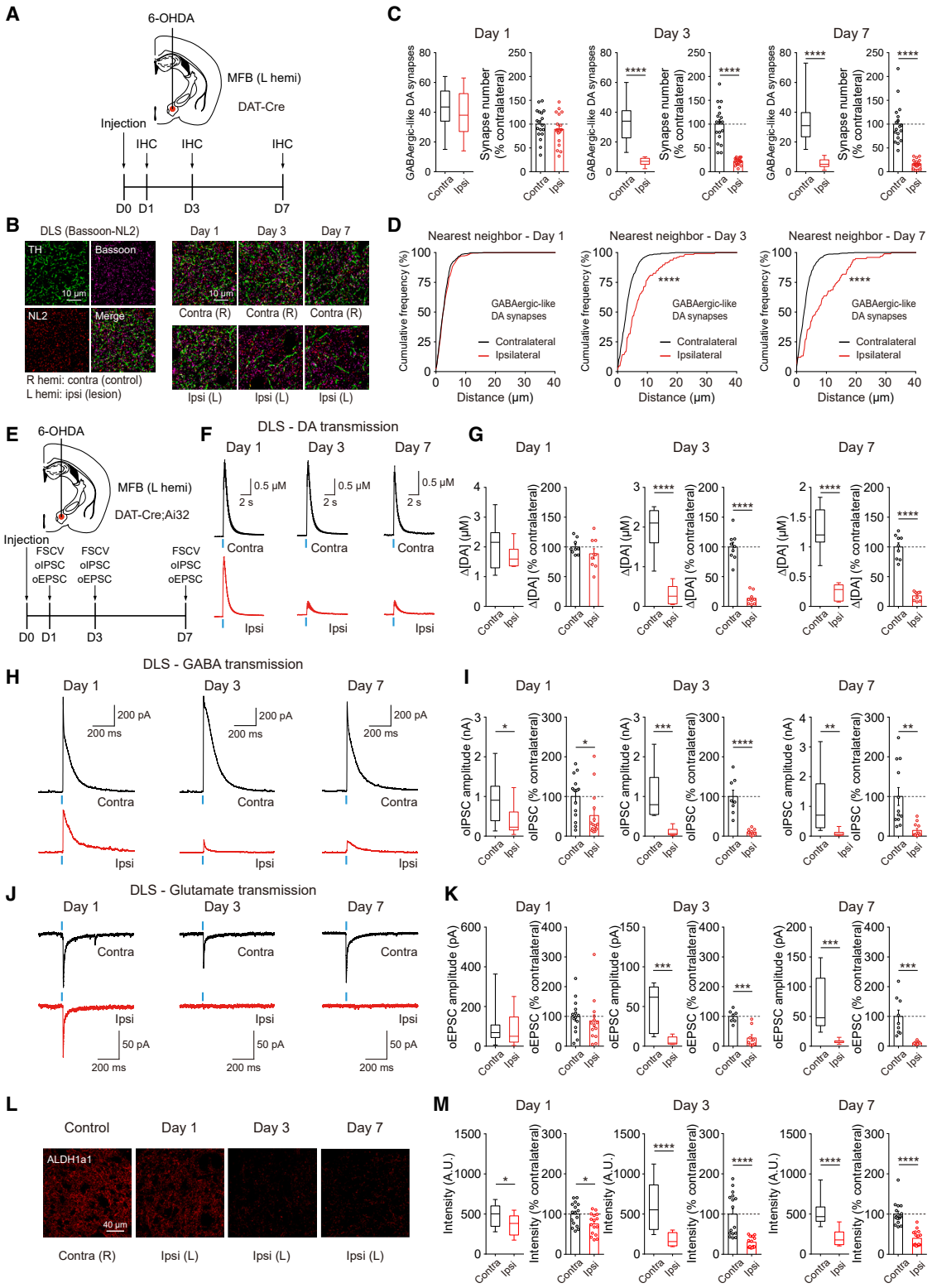


**Figure 6. The weakening of GABA co-transmission precedes the deficit of DA transmission at DA synapses in the 6-OHDA-induced PD model**

(A) Schematic illustration describing the injection of 6-OHDA into the MFB (left hemisphere) of DAT-Cre mice.

(B) Enhanced confocal images of GABAergic-like DA synapses (1-, 3-, and 7-day 6-OHDA incubation).

(C) Summary statistics for the number of GABAergic-like DA synapses (n = 18 images).

*(legend continued on next page)*

and 7H). However, the number of GABAergic-like DA synapses, DA transmission, and glutamate co-transmission decreased at a later time point (4 weeks after AAVs injection) (Figures 7B–7F and 7I–7J). Taken together, our findings reveal that the weakening of GABA transmission at DA synapses can precede other physiological and cellular changes including DA transmission and the number of GABAergic-like DA synapses in animal models of PD, which may be caused by the rapid reduction of ALDH1a1 in DA neurons.

## DISCUSSION

Electron microscopy studies have shown that DA terminals immunoreactive for TH make symmetrical contacts with striatal SPNs.[36,42] NL2 and Gephyrin, major postsynaptic proteins exclusively found at inhibitory synapses, were recently reported to exist at postsynaptic sites of striatal DA synapses.[4] In addition, it appears that GABA along with DA is co-transmitted at striatal DA synapses from DA terminals,[6,7] and we previously showed that dopaminergic GABA can be synthesized in midbrain DA neurons via non-canonical GABA synthesis pathway.[7] Here, we demonstrate that there exist structurally and functionally GABAergic-like DA synapses in the brain. Our results first show the strong correlation between DA and GABA transmission at DA synapses in both nigrostriatal and mesocorticolimbic pathways. GABA in DA neurons can be loaded into dopaminergic synaptic vesicles through VMAT2, a vesicular membrane protein for transporting DA from the cytosol into synaptic vesicles.[6,43] As such, it is reasonable to think that DA and GABA can be co-transmitted together from a considerable population of DA synapses in the brain. Our results are also roughly consistent with the previous observation that about 30% of DA varicosities, which contain Bassoon, can release DA in the striatum.[5] Notably, both DA and GABA transmission at DA synapses exhibit a much higher correlation with the number of GABAergic-like DA synapses identified by Bassoon than with that of GABAergic-like DA synapses by VMAT2. These results indicate that Bassoon is a more reliable presynaptic marker for GABAergic-like DA synapses that can co-transmit DA and GABA. However, it bears mentioning that there still remain many portions of dopaminergic presynaptic boutons that are not co-localized with inhibitory postsynaptic markers such as NL2 and Gephyrin. Those DA boutons may (or may not) release DA, glutamate, or both.[36]

Unlike DA axons immunoreactive for TH and DAT, these GABAergic-like DA synapses exhibit marked regional and spatial heterogeneity in the brain, especially within the striatum. GABAergic-like DA synapses also show region-specific clustering in the striatal subregions. This spatial heterogeneity is well suited to provide regionally distinct functions of DA synapses throughout the brain. Importantly, the density of GABAergic-like DA synapses is the highest in the DLS within the striatum, while OT and DMS display a relatively higher degree of clustering than DLS. Although the region-specific structure of neural circuits may partly underlie the high degree of clustering of GABAergic-like DA synapses in the OT, the relative difference of spatial clustering of GABAergic-like DA synapses between DLS and DMS might have physiological implications in diverse functions mediated by DLS and DMS. Furthermore, the spatial distribution of GABAergic-like DA synapses on the dendrite and the distinct physiological features of GABA co-transmission at DA synapses might contribute to the functional specificity of these synapses in regulating postsynaptic neurons.

Our data suggest that DA transmission in the brain, if not always, may accompany GABA transmission with high fidelity at GABAergic-like DA synapses. Although DA transmission under certain conditions can also provide spatially and temporally precise coding,[5,44] the co-transmission of GABA at DA synapses, in conjunction with glutamate, can reliably convey not only fast, but also synapse-specific and more precise signals to postsynaptic neurons. GABA co-transmission can be utilized to mark salient events with high temporal resolution.[9] On the other hand, depending on the intracellular concentration of $Cl^-$ in postsynaptic neurons, GABA co-transmission may also confer on DA synapses the ability to subtly modulate the excitation of subcellular regions of a postsynaptic neuron. Therefore, a distinct combination of DA and GABA transmission, and region-specific spatial distribution of GABAergic-like DA synapses, may provide critical repertoire to finely tune various types of target neurons for the appropriate movements and reward-related behaviors.

In the recent study by Uchigashima et al.,[4] the authors examined the effect of NL2 KD on striatal neurons by injecting microRNA-based lentivirus in the striatum of newborn pups. They reported that DA synapses identified by the co-localization of TH, Gephyrin, and GFP, are decreased in striatal SPNs by NL2 KD. Aside from differences in experimental details, however, this study underestimated the existence of GABA co-transmission at DA synapses, emphasizing only the identification of GABAergic postsynaptic molecules at DA synapses, and did not examine the physiological consequences of NL2 KD at DA synapses. Interestingly, we found that, although the expression level of NL2 is significantly reduced by short-term KD (6 weeks) of NL2 in striatal neurons, GABA transmission is highly elevated at DA synapses, while both DA transmission and GABAergic-like DA synapses are considerably diminished. Previous studies have demonstrated that the inhibitory neurotransmitter GABA itself is necessary for maintaining GABAergic synapses in the brain.[45–47] Thus, our findings raise the intriguing possibility that

(D) Cumulative frequency for the nearest neighbor distance of GABAergic-like DA synapses.
(E) Schematics illustrating the injection of 6-OHDA into the MFB (left hemisphere) of DAT-Cre;Ai32 mice.
(F and G) Representative recording traces and summary statistics of DA transmission at DA synapses (n = 9 slices).
(H and I) Representative recording traces and summary statistics of GABA transmission at DA synapses (n = 8–15 cells).
(J and K) Representative recording traces and summary statistics of glutamate transmission at DA synapses (n = 7–14 cells).
(L) Confocal images of ALDH1a1 in the DLS of 6-OHDA-injected mice.
(M) Summary statistics of ALDH1a1 intensity (n = 16 images). Data are presented as box and whisker plots or mean ± SEM. *p < 0.05, **p < 0.01, ***p < 0.001, ****p < 0.0001. See also Figure S7 and Table S1.

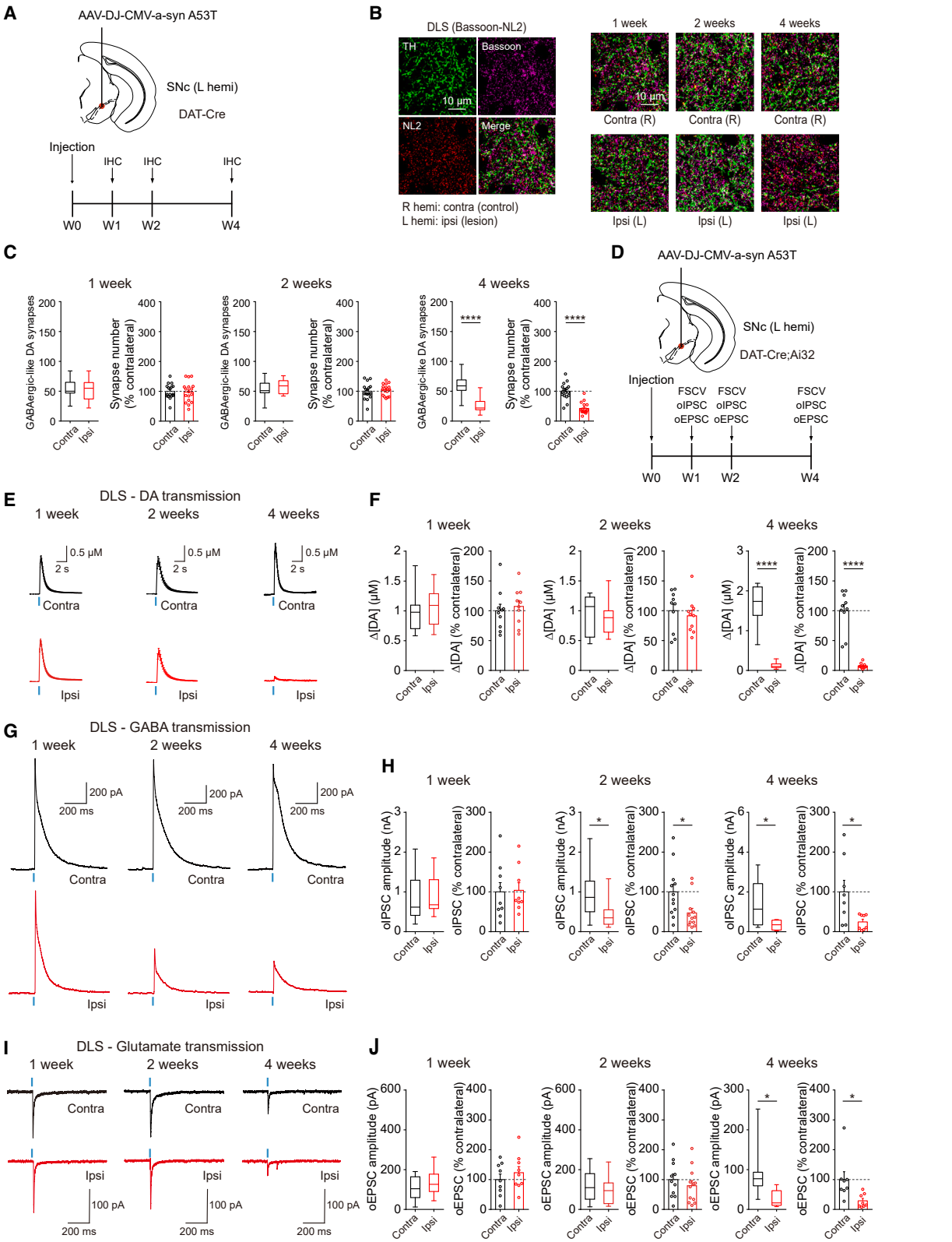


*(legend on next page)*

persistent GABA transmission *per se* might be essential for maintaining and stabilizing DA synapses by playing a trophic role. In addition, it is conceivable that GABA transmission at DA synapses may be enhanced to compensate for the loss of GABAergic-like DA synapses by short-term KD of NL2.[48] Notably, short-term NL2 KD did not seem to alter the postsynaptic expression of $GABA_AR$ or the quantal amplitude of GABA transmission at DA synapses. Instead, it increased the presynaptic release of GABA and the size of the remaining presynaptic boutons at GABAergic-like DA synapses, indicating that the compensatory effects at DA synapses caused by short-term KD of NL2 in striatal neurons are presynaptic, not postsynaptic.[49] Our findings further showed that these compensatory effects are temporary and long-term (12 weeks) KD of NL2 eventually downregulates not only GABA co-transmission but also glutamate co-transmission at DA synapses. Therefore, these results strongly support the importance of NL2 and GABA co-transmission in maintaining GABAergic-like DA synapses.

In mouse models of PD, the attenuation of GABA transmission precedes the impairments of DA and glutamate transmission at DA synapses. GABA transmission begins to alter when GABAergic-like DA synapses are intact by 6-OHDA injection or α-synuclein-expressing AAV injection. These results strongly suggest that GABA co-transmission at DA synapses may temporally undergo different pathological processes in the degeneration of the DA system. Moreover, it might be more susceptible to PD, potentially due to the early reduction of ALDH1a1, which is caused by PD-related neurotoxicity and oxidative stress.[50–52] GABA transporter 1 (GAT1) is also reported to contribute to GABA co-transmission at DA synapses, and future studies are needed to reveal the potential role of GAT1 in the early attenuation of GABA co-transmission at DA synapses in mouse models of PD.[53] Considered together, our results establish a comprehensive landscape of GABAergic-like DA synapses throughout the brain. In addition, our findings that a significant population of DA synapses is structurally and functionally GABAergic in the brain open numerous doors to a deeper mechanistic understanding of synaptic actions at DA synapses in health and disease.

### Limitations of the study

Although we tried to maximize the image resolution by using enhanced airyscan confocal microscopy, this method still has optical limitations in fully identifying the localization of synaptic molecules at GABAergic-like DA synapses. Future studies employing super-resolution imaging such as expansion microscopy or stochastic optical reconstruction microscopy might help give better insights into the molecular determinants of GABAergic-like DA synapses. In this study, we reconfirmed that NL2 exists at the postsynaptic sites of GABAergic-like DA synapses, and demonstrated that NL2 is critical for maintaining the structure and function of GABAergic-like DA synapses. However, there are more proteins including cell adhesion molecules, scaffolding proteins, and ion channels that comprise the pre- and post-synaptic compartments of conventional GABAergic synapses. Therefore, in case other GABAergic synaptic proteins are also present at DA synapses, the functional roles of these proteins at DA synapses should be further investigated to fully delineate the molecular mechanisms maintaining DA synapses. Finally, we found that short-term (6 weeks) KD of NL2 in striatal SPNs transiently facilitates GABA co-transmission through the potential increase in presynaptic release probability and hence reasoned that this enhanced GABA co-transmission might be a compensatory mechanism to attenuate the degeneration of DA synapses caused by NL2 KD. However, much remains to be clarified about how the postsynaptic short-term KD of NL2 in SPNs leads to selective facilitation of GABA co-transmission at DA terminals. Further investigation into the mechanisms behind this finding will be crucial to understand how DA synapses are functionally maintained in health and disease.

## STAR★METHODS

Detailed methods are provided in the online version of this paper and include the following:

- KEY RESOURCES TABLE
- RESOURCE AVAILABILITY
  - Lead contact
  - Materials availability
  - Data and code availability
- EXPERIMENTAL MODEL AND STUDY PARTICIPANT DETAILS
  - Animals
- METHOD DETAILS
  - Immunohistochemistry and confocal (enhanced confocal) imaging
  - Expansion microscopy
  - dLight dopamine imaging
  - Brain slice preparation for electrophysiology
  - Electrophysiology, optogenetic stimulation, and pharmacology
  - Fast-scanning cyclic voltammetry (FSCV)
  - Virus purchase

**Figure 7. The consistent early decline of GABA co-transmission in α-synuclein (A53T)-induced PD model**

(A) Schematic illustration describing the injection of α-synuclein (A53T) virus into the SNc (left hemisphere) of DAT-Cre mice.

(B) Enhanced confocal images of GABAergic-like DA synapses from the DLS in DAT-Cre mice injected with the α-synuclein virus (expressed for 1, 2, and 4 weeks).

(C) Summary statistics for the number of GABAergic-like DA synapses (n = 16–17 images).

(D) Schematics illustrating the injection of α-synuclein virus (A53T) into the SNc (left hemisphere) of DAT-Cre;Ai32 mice.

(E and F) Representative recording traces and summary statistics of DA transmission at DA synapses (n = 10 slices).

(G and H) Representative recording traces and summary statistics of GABA transmission at DA synapses (n = 8–12 cells).

(I and J) Representative recording traces and summary statistics of glutamate transmission at DA synapses (n = 8–12 cells). Data are presented as box and whisker plots or mean ± SEM. *p < 0.05, ****p < 0.0001. See also Table S1.

- shRNA expression and verification of shRNA-mediated knockdown of NLGN2 (NL2)
- α-synuclein-expressing AAV generation
- Quantitative real-time PCR
- AAV cloning and production
- Stereotaxic viral injection for sparse labeling
- Stereotaxic viral injection for NLGN2 (NL2) knockdown
- Stereotaxic 6-OHDA injection
- Stereotaxic α-synuclein-expressing AAV injection
- Stereotaxic viral injection for DREADDs

● QUANTIFICATION AND STATISTICAL ANALYSIS

- Spot detection and synapse extraction analysis (used for synapse analysis)
- dLight dopamine analysis
- Point pattern analysis
- Diggle-Cressie-Loosmore-Ford (DCLF) test
- Statistics

## SUPPLEMENTAL INFORMATION

Supplemental information can be found online at https://doi.org/10.1016/j.celrep.2023.113239.

## ACKNOWLEDGMENTS

We thank Dr. Dougu Nam (UNIST) and the members of Kim laboratory for helpful discussions. We also thank Dr. Christopher Ford (University of Colorado) for generously allowing us to use mGIRK2 AAVs. M.R. would like to thank Dr. David DiGregorio for suggestions and guidance. This research was supported by the Basic Science Research Program through the National Research Foundation of Korea (NRF) funded by the Ministry of Science and ICT (2017M3C7A1044966 to J.-H.P., and 2017R1C1B3005476, 2021R1A4A1031644, 2021M3A9G8022960, 2022M325E8017907, and 2023R1A2C1006489 to J.-I.K.), the POSCO Science Fellowship of POSCO TJ Park Foundation (to J.-I.K.), the intramural research fund of UNIST (1.210115.01 to J.-I.K.), and the Institute for Basic Science (IBS-R022-D1 to K.M.). Figures S2A and S2D were created with biorender.com.

## AUTHOR CONTRIBUTIONS

Conceptualization: H.-J.K. and J.-I.K.; methodology, H.-J.K., B.H., M.R., J.L., B.E.L., Y.L., E.J.C., M.J., S.E.L., K.M., J.-H.B., J.-H.P., and J.-I.K.; investigation, H.-J.K., M.R., J.L., B.E.L., Y.L., E.J.C., M.J., and J.-I.K.; interpretation of data, H.-J.K., M.R., J.-H.B., and J.-I.K.; writing – original draft, H.-J.K. and J.-I.K.; writing – review & editing, H.-J.K., M.R., J.-H.B., and J.-I.K.; funding acquisition, K.M., J.-H.P., and J.-I.K.; supervision, J.-I.K.

## DECLARATION OF INTERESTS

The authors declare no competing interests.

## INCLUSION AND DIVERSITY

We worked to ensure sex balance in the selection of non-human subjects. While citing references scientifically relevant for this work, we also actively worked to promote gender balance in our reference list.

Received: March 11, 2023
Revised: August 18, 2023
Accepted: September 25, 2023
Published: October 17, 2023

## REFERENCES

1. Schultz, W. (2007). Multiple dopamine functions at different time courses. Annu. Rev. Neurosci. *30*, 259–288. https://doi.org/10.1146/annurev.neuro.28.061604.135722.
2. Berke, J.D. (2018). What does dopamine mean? Nat. Neurosci. *21*, 787–793. https://doi.org/10.1038/s41593-018-0152-y.
3. Smiley, J.F., Levey, A.I., Ciliax, B.J., and Goldman-Rakic, P.S. (1994). D1 dopamine receptor immunoreactivity in human and monkey cerebral cortex: predominant and extrasynaptic localization in dendritic spines. Proc. Natl. Acad. Sci. USA *91*, 5720–5724. https://doi.org/10.1073/pnas.91.12.5720.
4. Uchigashima, M., Ohtsuka, T., Kobayashi, K., and Watanabe, M. (2016). Dopamine synapse is a neuroligin-2-mediated contact between dopaminergic presynaptic and GABAergic postsynaptic structures. Proc. Natl. Acad. Sci. USA *113*, 4206–4211. https://doi.org/10.1073/pnas.1514074113.
5. Liu, C., Kershberg, L., Wang, J., Schneeberger, S., and Kaeser, P.S. (2018). Dopamine Secretion Is Mediated by Sparse Active Zone-like Release Sites. Cell *172*, 706–718.e15. https://doi.org/10.1016/j.cell.2018.01.008.
6. Tritsch, N.X., Ding, J.B., and Sabatini, B.L. (2012). Dopaminergic neurons inhibit striatal output through non-canonical release of GABA. Nature *490*, 262–266. https://doi.org/10.1038/nature11466.
7. Kim, J.I., Ganesan, S., Luo, S.X., Wu, Y.W., Park, E., Huang, E.J., Chen, L., and Ding, J.B. (2015). Aldehyde dehydrogenase 1a1 mediates a GABA synthesis pathway in midbrain dopaminergic neurons. Science *350*, 102–106. https://doi.org/10.1126/science.aac4690.
8. Stuber, G.D., Hnasko, T.S., Britt, J.P., Edwards, R.H., and Bonci, A. (2010). Dopaminergic terminals in the nucleus accumbens but not the dorsal striatum corelease glutamate. J. Neurosci. *30*, 8229–8233. https://doi.org/10.1523/JNEUROSCI.1754-10.2010.
9. Tritsch, N.X., Granger, A.J., and Sabatini, B.L. (2016). Mechanisms and functions of GABA co-release. Nat. Rev. Neurosci. *17*, 139–145. https://doi.org/10.1038/nrn.2015.21.
10. Matsuda, W., Furuta, T., Nakamura, K.C., Hioki, H., Fujiyama, F., Arai, R., and Kaneko, T. (2009). Single nigrostriatal dopaminergic neurons form widely spread and highly dense axonal arborizations in the neostriatum. J. Neurosci. *29*, 444–453. https://doi.org/10.1523/JNEUROSCI.4029-08.2009.
11. Rommelfanger, K.S., and Wichmann, T. (2010). Extrastriatal dopaminergic circuits of the Basal Ganglia. Front. Neuroanat. *4*, 139. https://doi.org/10.3389/fnana.2010.00139.
12. Cragg, S.J. (2003). Variable dopamine release probability and short-term plasticity between functional domains of the primate striatum. J. Neurosci. *23*, 4378–4385.
13. Janezic, S., Threlfell, S., Dodson, P.D., Dowie, M.J., Taylor, T.N., Potgieter, D., Parkkinen, L., Senior, S.L., Anwar, S., Ryan, B., et al. (2013). Deficits in dopaminergic transmission precede neuron loss and dysfunction in a new Parkinson model. Proc. Natl. Acad. Sci. USA *110*, E4016–E4025. https://doi.org/10.1073/pnas.1309143110.
14. Yung, K.K., Bolam, J.P., Smith, A.D., Hersch, S.M., Ciliax, B.J., and Levey, A.I. (1995). Immunocytochemical localization of D1 and D2 dopamine receptors in the basal ganglia of the rat: light and electron microscopy. Neuroscience *65*, 709–730. https://doi.org/10.1016/0306-4522(94)00536-e.
15. Varoqueaux, F., Jamain, S., and Brose, N. (2004). Neuroligin 2 is exclusively localized to inhibitory synapses. Eur. J. Cell Biol. *83*, 449–456. https://doi.org/10.1078/0171-9335-00410.
16. Banerjee, A., Lee, J., Nemcova, P., Liu, C., and Kaeser, P.S. (2020). Synaptotagmin-1 is the Ca(2+) sensor for fast striatal dopamine release. Elife *9*, e58359. https://doi.org/10.7554/eLife.58359.
17. Asano, S.M., Gao, R., Wassie, A.T., Tillberg, P.W., Chen, F., and Boyden, E.S. (2018). Expansion Microscopy: Protocols for Imaging Proteins and

RNA in Cells and Tissues. Curr. Protoc. Cell Biol. *80*, e56. https://doi.org/10.1002/cpcb.56.

18. Tyagarajan, S.K., and Fritschy, J.M. (2014). Gephyrin: a master regulator of neuronal function? Nat. Rev. Neurosci. *15*, 141–156. https://doi.org/10.1038/nrn3670.
19. Sassoè-Pognetto, M., and Fritschy, J.M. (2000). Mini-review: gephyrin, a major postsynaptic protein of GABAergic synapses. Eur. J. Neurosci. *12*, 2205–2210. https://doi.org/10.1046/j.1460-9568.2000.00106.x.
20. Perin, R., Berger, T.K., and Markram, H. (2011). A synaptic organizing principle for cortical neuronal groups. Proc. Natl. Acad. Sci. USA *108*, 5419–5424. https://doi.org/10.1073/pnas.1016051108.
21. Druckmann, S., Feng, L., Lee, B., Yook, C., Zhao, T., Magee, J.C., and Kim, J. (2014). Structured synaptic connectivity between hippocampal regions. Neuron *81*, 629–640. https://doi.org/10.1016/j.neuron.2013.11.026.
22. Kiskowski, M.A., Hancock, J.F., and Kenworthy, A.K. (2009). On the use of Ripley's K-function and its derivatives to analyze domain size. Biophys. J. *97*, 1095–1103. https://doi.org/10.1016/j.bpj.2009.05.039.
23. Rebola, N., Reva, M., Kirizs, T., Szoboszlay, M., Lőrincz, A., Moneron, G., Nusser, Z., and DiGregorio, D.A. (2019). Distinct Nanoscale Calcium Channel and Synaptic Vesicle Topographies Contribute to the Diversity of Synaptic Function. Neuron *104*, 693–710.e9. https://doi.org/10.1016/j.neuron.2019.08.014.
24. Loosmore, N.B., and Ford, E.D. (2006). Statistical inference using the g or K point pattern spatial statistics. Ecology *87*, 1925–1931. https://doi.org/10.1890/0012-9658(2006)87[1925:siutgo]2.0.co;2.
25. Kleindienst, T., Winnubst, J., Roth-Alpermann, C., Bonhoeffer, T., and Lohmann, C. (2011). Activity-dependent clustering of functional synaptic inputs on developing hippocampal dendrites. Neuron *72*, 1012–1024. https://doi.org/10.1016/j.neuron.2011.10.015.
26. Losonczy, A., and Magee, J.C. (2006). Integrative properties of radial oblique dendrites in hippocampal CA1 pyramidal neurons. Neuron *50*, 291–307. https://doi.org/10.1016/j.neuron.2006.03.016.
27. Linders, L.E., Supiot, L.F., Du, W., D'Angelo, R., Adan, R.A.H., Riga, D., and Meye, F.J. (2022). Studying Synaptic Connectivity and Strength with Optogenetics and Patch-Clamp Electrophysiology. Int. J. Mol. Sci. *23*, 11612. https://doi.org/10.3390/ijms231911612.
28. Ullrich, B., Li, C., Zhang, J.Z., McMahon, H., Anderson, R.G., Geppert, M., and Südhof, T.C. (1994). Functional properties of multiple synaptotagmins in brain. Neuron *13*, 1281–1291. https://doi.org/10.1016/0896-6273(94)90415-4.
29. Xu, J., Mashimo, T., and Südhof, T.C. (2007). Synaptotagmin-1, -2, and -9: Ca(2+) sensors for fast release that specify distinct presynaptic properties in subsets of neurons. Neuron *54*, 567–581. https://doi.org/10.1016/j.neuron.2007.05.004.
30. Chang, S., Trimbuch, T., and Rosenmund, C. (2018). Synaptotagmin-1 drives synchronous Ca(2+)-triggered fusion by C2B-domain-mediated synaptic-vesicle-membrane attachment. Nat. Neurosci. *21*, 33–40. https://doi.org/10.1038/s41593-017-0037-5.
31. Poulopoulos, A., Aramuni, G., Meyer, G., Soykan, T., Hoon, M., Papadopoulos, T., Zhang, M., Paarmann, I., Fuchs, C., Harvey, K., et al. (2009). Neuroligin 2 drives postsynaptic assembly at perisomatic inhibitory synapses through gephyrin and collybistin. Neuron *63*, 628–642. https://doi.org/10.1016/j.neuron.2009.08.023.
32. Chubykin, A.A., Atasoy, D., Etherton, M.R., Brose, N., Kavalali, E.T., Gibson, J.R., and Südhof, T.C. (2007). Activity-dependent validation of excitatory versus inhibitory synapses by neuroligin-1 versus neuroligin-2. Neuron *54*, 919–931. https://doi.org/10.1016/j.neuron.2007.05.029.
33. Nguyen, Q.A., Horn, M.E., and Nicoll, R.A. (2016). Distinct roles for extracellular and intracellular domains in neuroligin function at inhibitory synapses. Elife *5*, e19236. https://doi.org/10.7554/eLife.19236.
34. Bekkers, J.M., and Clements, J.D. (1999). Quantal amplitude and quantal variance of strontium-induced asynchronous EPSCs in rat dentate granule neurons. J. Physiol. *516*, 227–248. https://doi.org/10.1111/j.1469-7793.1999.227aa.x.
35. Zych, S.M., and Ford, C.P. (2022). Divergent properties and independent regulation of striatal dopamine and GABA co-transmission. Cell Rep. *39*, 110823. https://doi.org/10.1016/j.celrep.2022.110823.
36. Zhang, S., Qi, J., Li, X., Wang, H.L., Britt, J.P., Hoffman, A.F., Bonci, A., Lupica, C.R., and Morales, M. (2015). Dopaminergic and glutamatergic microdomains in a subset of rodent mesoaccumbens axons. Nat. Neurosci. *18*, 386–392. https://doi.org/10.1038/nn.3945.
37. Subramaniam, M., Althof, D., Gispert, S., Schwenk, J., Auburger, G., Kulik, A., Fakler, B., and Roeper, J. (2014). Mutant alpha-synuclein enhances firing frequencies in dopamine substantia nigra neurons by oxidative impairment of A-type potassium channels. J. Neurosci. *34*, 13586–13599. https://doi.org/10.1523/JNEUROSCI.5069-13.2014.
38. Patriarchi, T., Cho, J.R., Merten, K., Howe, M.W., Marley, A., Xiong, W.H., Folk, R.W., Broussard, G.J., Liang, R., Jang, M.J., et al. (2018). Ultrafast neuronal imaging of dopamine dynamics with designed genetically encoded sensors. Science *360*, eaat4422. https://doi.org/10.1126/science.aat4422.
39. Galter, D., Buervenich, S., Carmine, A., Anvret, M., and Olson, L. (2003). ALDH1 mRNA: presence in human dopamine neurons and decreases in substantia nigra in Parkinson's disease and in the ventral tegmental area in schizophrenia. Neurobiol. Dis. *14*, 637–647. https://doi.org/10.1016/j.nbd.2003.09.001.
40. Grünblatt, E., Ruder, J., Monoranu, C.M., Riederer, P., Youdim, M.B., and Mandel, S.A. (2018). Differential Alterations in Metabolism and Proteolysis-Related Proteins in Human Parkinson's Disease Substantia Nigra. Neurotox. Res. *33*, 560–568. https://doi.org/10.1007/s12640-017-9843-5.
41. Carmichael, K., Evans, R.C., Lopez, E., Sun, L., Kumar, M., Ding, J., Khaliq, Z.M., and Cai, H. (2021). Function and Regulation of ALDH1A1-Positive Nigrostriatal Dopaminergic Neurons in Motor Control and Parkinson's Disease. Front. Neural Circ. *15*, 644776. https://doi.org/10.3389/fncir.2021.644776.
42. Moss, J., and Bolam, J.P. (2008). A dopaminergic axon lattice in the striatum and its relationship with cortical and thalamic terminals. J. Neurosci. *28*, 11221–11230. https://doi.org/10.1523/JNEUROSCI.2780-08.2008.
43. Stensrud, M.J., Puchades, M., and Gundersen, V. (2014). GABA is localized in dopaminergic synaptic vesicles in the rodent striatum. Brain Struct. Funct. *219*, 1901–1912. https://doi.org/10.1007/s00429-013-0609-4.
44. Arbuthnott, G.W., and Wickens, J. (2007). Space, time and dopamine. Trends Neurosci. *30*, 62–69. https://doi.org/10.1016/j.tins.2006.12.003.
45. Huang, Z.J., Di Cristo, G., and Ango, F. (2007). Development of GABA innervation in the cerebral and cerebellar cortices. Nat. Rev. Neurosci. *8*, 673–686. https://doi.org/10.1038/nrn2188.
46. Chattopadhyaya, B., Di Cristo, G., Wu, C.Z., Knott, G., Kuhlman, S., Fu, Y., Palmiter, R.D., and Huang, Z.J. (2007). GAD67-mediated GABA synthesis and signaling regulate inhibitory synaptic innervation in the visual cortex. Neuron *54*, 889–903. https://doi.org/10.1016/j.neuron.2007.05.015.
47. Oh, W.C., Lutzu, S., Castillo, P.E., and Kwon, H.B. (2016). De novo synaptogenesis induced by GABA in the developing mouse cortex. Science *353*, 1037–1040. https://doi.org/10.1126/science.aaf5206.
48. Pozo, K., and Goda, Y. (2010). Unraveling mechanisms of homeostatic synaptic plasticity. Neuron *66*, 337–351. https://doi.org/10.1016/j.neuron.2010.04.028.
49. Huang, Z.J., and Scheiffele, P. (2008). GABA and neuroligin signaling: linking synaptic activity and adhesion in inhibitory synapse development. Curr. Opin. Neurobiol. *18*, 77–83. https://doi.org/10.1016/j.conb.2008.05.008.
50. Goldstein, D.S., Kopin, I.J., and Sharabi, Y. (2014). Catecholamine autotoxicity. Implications for pharmacology and therapeutics of Parkinson disease and related disorders. Pharmacol. Ther. *144*, 268–282. https://doi.org/10.1016/j.pharmthera.2014.06.006.

51. Cai, H., Liu, G., Sun, L., and Ding, J. (2014). Aldehyde Dehydrogenase 1 making molecular inroads into the differential vulnerability of nigrostriatal dopaminergic neuron subtypes in Parkinson's disease. Transl. Neurodegener. *3*, 27. https://doi.org/10.1186/2047-9158-3-27.

52. Masato, A., Plotegher, N., Boassa, D., and Bubacco, L. (2019). Impaired dopamine metabolism in Parkinson's disease pathogenesis. Mol. Neurodegener. *14*, 35. https://doi.org/10.1186/s13024-019-0332-6.

53. Tritsch, N.X., Oh, W.J., Gu, C., and Sabatini, B.L. (2014). Midbrain dopamine neurons sustain inhibitory transmission using plasma membrane uptake of GABA, not synthesis. Elife *3*, e01936. https://doi.org/10.7554/eLife.01936.

54. Lee, B.E., Kim, H.Y., Kim, H.J., Jeong, H., Kim, B.G., Lee, H.E., Lee, J., Kim, H.B., Lee, S.E., Yang, Y.R., et al. (2020). O-GlcNAcylation regulates dopamine neuron function, survival and degeneration in Parkinson disease. Brain *143*, 3699–3716. https://doi.org/10.1093/brain/awaa320.

55. Liu, C., Cai, X., Ritzau-Jost, A., Kramer, P.F., Li, Y., Khaliq, Z.M., Hallermann, S., and Kaeser, P.S. (2022). An action potential initiation mechanism in distal axons for the control of dopamine release. Science *375*, 1378–1385. https://doi.org/10.1126/science.abn0532.

56. Ventura, A., Meissner, A., Dillon, C.P., McManus, M., Sharp, P.A., Van Parijs, L., Jaenisch, R., and Jacks, T. (2004). Cre-lox-regulated conditional RNA interference from transgenes. Proc. Natl. Acad. Sci. USA *101*, 10380–10385. https://doi.org/10.1073/pnas.0403954101.

57. Park, J., Throop, A.L., and LaBaer, J. (2015). Site-specific recombinational cloning using gateway and in-fusion cloning schemes. Curr. Protoc. Mol. Biol. *110*, 3.20.1–3.20.23. https://doi.org/10.1002/0471142727.mb0320s110.

58. Livak, K.J., and Schmittgen, T.D. (2001). Analysis of relative gene expression data using real-time quantitative PCR and the 2(-Delta Delta C(T)) Method. Methods *25*, 402–408. https://doi.org/10.1006/meth.2001.1262.

59. Smal, I., Loog, M., Niessen, W., and Meijering, E. (2010). Quantitative comparison of spot detection methods in fluorescence microscopy. IEEE Trans. Med. Imag. *29*, 282–301. https://doi.org/10.1109/TMI.2009.2025127.

60. Kimori, Y., Baba, N., and Morone, N. (2010). Extended morphological processing: a practical method for automatic spot detection of biological markers from microscopic images. BMC Bioinf. *11*, 373. https://doi.org/10.1186/1471-2105-11-373.

61. Aishwarya, N., Phamila, Y.A.V., and Amutha, R. (2013). Multi-focus image fusion using multi-structure top-hat transform and image variance*3–5*, pp. 352–356.

62. Ripley, B.D. (1977). Modeling Spatial Patterns. J. Roy. Stat. Soc. B *39*, 172–192.

63. (1977). Discussion on Dr Ripley's Paper. J. Roy. Stat. Soc. B *39*, 192–212. https://doi.org/10.1111/j.2517-6161.1977.tb01616.x.

64. Diggle, P. (2003). The Statistical Analysis of Spatial Point Patterns.

## STAR★METHODS

### KEY RESOURCES TABLE

| REAGENT or RESOURCE | SOURCE | IDENTIFIER |
|---|---|---|
| Antibodies | | |
| Rabbit polyclonal anti-tyrosine hydroxylase | Abcam | Cat# ab112; RRID: AB_297840 |
| Chicken polyclonal anti-tyrosine hydroxylase | Abcam | Cat# ab76442; RRID: AB_1524535 |
| Rat monoclonal anti-dopamine transporter | Abcam | Cat# ab5990; RRID: AB_305226 |
| Rabbit polyclonal anti-VMAT2 | Nittobo Medical | Cat# VMAT2-Rb-Af720; RRID: AB_2571857 |
| Mouse monoclonal anti-gephyrin | Synaptic Systems | Cat# 147 111; RRID: AB_887719 |
| Mouse monoclonal anti-RFP | Thermo Fisher Scientific | Cat# MA5-15257; RRID: AB_10999796 |
| Chicken polyclonal anti-GFP | Aves Labs | Cat# GFP-1010; RRID: AB_2307313 |
| Guinea pig polyclonal anti-bassoon | Synaptic Systems | Cat# 141 004; RRID: AB_2290619 |
| Mouse monoclonal anti-bassoon | Enzo Life Sciences | Cat# ADI-VAM-PS003-D; RRID: AB_2038857 |
| Guinea pig polyclonal anti-neuroligin 2 | Nittobo Medical | Cat# Nlgn2-GP-Af760; RRID: AB_2571609 |
| Rabbit polyclonal anti-VGAT | Synaptic Systems | Cat# 131 003; RRID: AB_887869 |
| Guinea pig polyclonal anti-VGAT | Synaptic Systems | Cat# 131 005; RRID: AB_1106810 |
| Mouse monoclonal anti-synaptotagmin 1 | Synaptic Systems | Cat# 105 011; RRID: AB_887832 |
| Rabbit polyclonal anti-synaptotagmin 7 | Synaptic Systems | Cat# 105 173; RRID: AB_887838 |
| Rabbit polyclonal anti-synaptotagmin 5/9 | Synaptic Systems | Cat# 105 053; RRID: AB_2199639 |
| Rabbit polyclonal anti-ALDH1a1 | Sigma-Aldrich | Cat# HPA002123; RRID: AB_1844722 |
| Rabbit polyclonal anti-VGLUT2 | Synaptic Systems | Cat# 135 403; RRID: AB_887883 |
| Mouse monoclonal anti-PSD95 | Millipore | Cat# MAB1596; RRID: AB_2092365 |
| Rabbit polyclonal anti-GABAARα1 | Nittobo Medical | Cat# GABAARa1-Rb-Af660; RRID: AB_2571571 |
| Goat anti-Rabbit IgG (H + L) Cross-Adsorbed Secondary Antibody, Alexa Fluor 405 | Invitrogen | Cat# A-31556; RRID: AB_221605 |
| Goat anti-Rabbit IgG (H + L) Cross-Adsorbed Secondary Antibody, Alexa Fluor 488 | Invitrogen | Cat# A-11008; RRID: AB_143165 |
| Goat anti-Rabbit IgG (H + L) Cross-Adsorbed Secondary Antibody, Alexa Fluor 594 | Invitrogen | Cat# A-11012; RRID: AB_2534079 |
| Goat anti-Rabbit IgG (H + L) Highly Cross-Adsorbed Secondary Antibody, Alexa Fluor 647 | Invitrogen | Cat# A-21245; RRID: AB_2535813 |
| Goat anti-Mouse IgG (H + L) Cross-Adsorbed Secondary Antibody, Alexa Fluor 488 | Invitrogen | Cat# A-11001; RRID: AB_2534069 |
| Goat anti-Mouse IgG (H + L) Cross-Adsorbed Secondary Antibody, Alexa Fluor 594 | Invitrogen | Cat# A-11005; RRID: AB_2534073 |
| Goat anti-Mouse IgG (H + L) Cross-Adsorbed Secondary Antibody, Alexa Fluor 647 | Invitrogen | Cat# A-21235; RRID: AB_2535804 |
| Goat anti-Rat IgG (H + L) Cross-Adsorbed Secondary Antibody, Alexa Fluor 594 | Invitrogen | Cat# A-11007; RRID: AB_10561522 |

(*Continued on next page*)

*Continued*

| REAGENT or RESOURCE | SOURCE | IDENTIFIER |
|---|---|---|
| Goat anti-Chicken IgG (H + L) Cross-Adsorbed Secondary Antibody, Alexa Fluor 405 | Abcam | Cat# ab175674; RRID: AB_2890171 |
| Goat anti-Chicken IgG (H + L) Cross-Adsorbed Secondary Antibody, Alexa Fluor 488 | Invitrogen | Cat# A-11039; RRID: AB_2534096 |
| Goat anti-Guinea pig IgG (H + L) Highly Cross-Adsorbed Secondary Antibody, Alexa Fluor 594 | Invitrogen | Cat# A-11076; RRID: AB_2534120 |
| Goat anti-Guinea pig IgG (H + L) Highly Cross-Adsorbed Secondary Antibody, Alexa Fluor 647 | Invitrogen | Cat# A-21450; RRID: AB_2735091 |
| **Bacterial and virus strains** | | |
| AAV-hSyn-GFP | UNC Vector Core | AV5075E |
| AAV-hSyn-DIO-mCherry | Addgene | 50459-AAV5 |
| AAV-U6-scrambled RNA-hSyn-mCherry | Korea Institute of Science and Technology (KIST) Virus Facility | N/A |
| AAV-U6-mNLGN2-shRNA-hSyn-mCherry | Korea Institute of Science and Technology (KIST) Virus Facility | N/A |
| AAV-Ef1a-DIO ChETA-EYFP | Addgene | 26968-AAV5 |
| AAV-hSyn-hM4D(Gi)-mCherry | Addgene | 50475-AAV5 |
| AAV-*syn*-dLight1.3b | Addgene | 135762-AAV9 |
| AAV9.hSyn.tdTomato.T2A.m.GirK2-1-A22A.WPRE.bGH | Upenn | V8414S |
| **Chemicals, peptides, and recombinant proteins** | | |
| Zoletil | Virbac Korea | N/A |
| Rompun | Bayer Korea | N/A |
| Paraformaldehyde | Sigma-Aldrich | Cat# 441244 |
| PBS | Fisher Scientific | Cat# BP399-500 |
| Normal goat serum | Gibco | Cat# 16210064 |
| Bovine serum albumin | Sigma-Aldrich | Cat# A7030 |
| ProLong™ Gold Antifade Mountant | Invitrogen | Cat# P10144 |
| Isoflurane | Piramal Critical Care | N/A |
| NNC 55-0396 | Alomone Labs | Cat# N-206 |
| ω-conotoxin | Alomone Labs | Cat# C-300 |
| ω-agatoxin | Alomone Labs | Cat# STA-500 |
| CNQX | Tocris | Cat# 0190 |
| D-AP5 | Tocris | Cat# 0106 |
| SR 95531 hydrobromide (Gabazine) | Tocris | Cat# 1262 |
| Strontium chloride hexahydrate | Sigma-Aldrich | Cat# 255521 |
| Dopamine hydrochloride | Tocris | Cat# 3548 |
| RNA extraction kit | Intron Bio | Cat# 17221 |
| In-Fusion® HD cloning kit | Clontech | Cat# 639648 |
| 6-((acryloyl)amino)hexanoic Acid, Succinimidyl Ester | Invitrogen | Cat# A20770 |
| Sodium acrylate | Sigma-Aldrich | Cat# 408220 |
| Acrylamide | Sigma-Aldrich | Cat# A9099 |
| N,N′-Methylenebis(acrylamide) | Sigma-Aldrich | Cat# 146072 |
| Tetramethylethylenediamine (TEMED) | Biorad | Cat# 1610801 |

(*Continued on next page*)

*Continued*

| REAGENT or RESOURCE | SOURCE | IDENTIFIER |
|---|---|---|
| Ammonium persulfate | Sigma-Aldrich | Cat# 248614 |
| Triton X-100 | Sigma-Aldrich | Cat# X100 |
| Ethylenediaminetetraacetic acid | Sigma-Aldrich | Cat# E9884 |
| Tris (1M) aqueous solution, pH 8 | Intron bio | Cat# IBS-BT019 |
| Proteinase K | Thermo Scientific | Cat# EO0491 |
| Poly-L-lysine solution | Sigma-Aldrich | Cat# P8920 |
| Clozapine N-oxide dihydrochloride | Tocris | Cat# 6329 |
| **Experimental models: Organisms/strains** | | |
| Mouse: DAT-Cre: B6.SJL-*Slc6a3*$^{tm1.1(cre)Bkmn}$/J | The Jackson Laboratory | JAX: 006660 |
| Mouse: Ai32: B6.Cg-*Gt(ROSA)26Sor*$^{tm32(CAG-COP4*H134R/EYFP)Hze}$/J | The Jackson Laboratory | JAX: 024109 |
| Mouse: A2A-Cre: B6.FVB(Cg)-Tg(Adora2a-cre)KG139Gsat/Mmucd | MMRRC | Stock #: 036158-UCD |
| **Recombinant DNA** | | |
| pSicoR-mCh-empty | Addgene | Cat# 21907 |
| pAAV-minCMV-mCherry | Addgene | Cat# 27970 |
| **Software and algorithms** | | |
| Zen software | Carl Zeiss | RRID: SCR_013672 |
| ImageJ | NIH | RRID: SCR_002285 |
| MATLAB | MathWorks | RRID: SCR_001622 |
| WinWCP | Strathclyde software | RRID: SCR_014713 |
| Clampfit 10.7 | Molecular Devices | RRID: SCR_011323 |
| OriginPro 2017 | OriginLab | RRID: SCR_014212 |
| Mini Analysis | Synaptosoft | RRID: SCR_002184 |
| GraphPad Prism version 10 | GraphPad software | RRID: SCR_002798 |
| Analysis codes | This paper | Zenodo: https://doi.org/10.5281/zenodo.8260324 |
| **Other** | | |
| SM2010 R Microtome | Leica | N/A |
| FV1000 confocal laser scanning microscope | Olympus | RRID: SCR_016840 |
| LSM780N multi-photon confocal laser scanning microscope | Carl Zeiss | N/A |
| LSM880 multi-photon confocal laser scanning microscope | Carl Zeiss | N/A |
| LSM980 multi-photon confocal laser scanning microscope | Carl Zeiss | N/A |
| VT1200S Vibratome | Leica | RRID: SCR_018453 |
| Fixed Stage Microscopes BX51WI | Olympus | N/A |
| Multiclamp 700B | Molecular Devices | RRID: SCR_018455 |
| NI PCIe-6259 Multifunction I/O Device | National Instruments | N/A |
| Blue diode laser | Opto Engine LLC | Cat# MDL-III-450 |
| Neutral density filter U-25ND6 | Olympus | N/A |
| Stereotaxic system | Stoelting | Cat# 51730 |
| P-1000 Micropipette puller | Sutter | RRID: SCR_021042 |
| ORCA-Flash4.0 V3 Digital CMOS camera | Hamamatsu | Cat# C13440-20CU |
| High-power LED for microscopy, 470nm (blue) | Thor labs | Cat# SOLIS-470C |

## RESOURCE AVAILABILITY

### Lead contact

Further information and requests for resources and reagents should be directed to and will be fulfilled by the lead contact, Jae-Ick Kim (jikim220@unist.ac.kr).

### Materials availability

All plasmids and viral vectors generated for the study can be obtained from the lead contact upon request.

### Data and code availability

All data will be shared by the lead contact upon request. All original code has been deposited at Zenodo and is publicly available as of the date of publication. DOIs are listed in the key resources table. Any additional information or code required to reanalyze the data reported in this paper is available from the lead contact upon request.

## EXPERIMENTAL MODEL AND STUDY PARTICIPANT DETAILS

### Animals

Adult (8–16 weeks, male and female) mice were used for this study. To generate dopaminergic neuron-specific ChR2 expressing mice, DAT-Cre (B6.SJL-*Slc6a3*$^{tm1.1(cre)Bkmn}$/J, Jackson stock number: 006660) mice were crossed with Ai32 (B6.Cg-*Gt(ROSA)26Sor*$^{tm32(CAG-COP4*H134R/EYFP)Hze}$/J, Jackson stock number: 024109) mice, producing DAT-Cre; Ai32 mice. These mice were used for optogenetic stimulation of dopaminergic terminals in whole-cell patch clamp recording and fast-scanning cyclic voltammetry (FSCV) experiments. DAT-Cre mice (and DAT-Cre; Ai32) were primarily used in immunohistochemistry and fluorescence imaging experiments. To generate indirect pathway spiny projection neuron (iSPN)-specific ChR2 expressing mice, A2A-Cre (B6.FVB(Cg)-Tg(Adora2a-cre)KG139Gsat/Mmucd, MMRRC stock number: 036158-UCD) mice were crossed with Ai32 mice, producing A2A-Cre; Ai32. These mice were used in whole-cell patch clamp recording and immunohistochemistry experiments. A2A-Cre mice were also used for immunohistochemistry and fluorescence imaging experiments. All mice were maintained in C57BL/6J background. The experiment was not blind to the genotypes of mice. Mice were group-housed (up to 5 mice per cage) and bred under standard pathogen-free housing conditions in the animal facility of Ulsan National Institute of Science and Technology (UNIST) on a 12-h light/dark cycle (lights on from 7 a.m. to 7 p.m.). Food and water were available *ad libitum*. All experimental procedures were conducted in accordance with protocols approved by the Institutional Animal Care and Utilization Committee of UNIST.

## METHOD DETAILS

### Immunohistochemistry and confocal (enhanced confocal) imaging

For immunofluorescence staining, mice were anesthetized by intraperitoneal injection of zoletil (60 mg/kg, Virbac Korea) and rompun (15 mg/kg, Bayer Korea) mixture solution (zoletil: rompun: saline = 4 : 1: 20) and perfused transcardially with phosphate buffer (PB), followed by 4% paraformaldehyde (PFA). Brains were rapidly removed and maintained in 4% PFA at 4°C for overnight.[54] Fixed brains were transferred to 30% sucrose in 0.01 M PB for cryoprotection. Brain sections containing striatum, cortex, and extrastriatal basal ganglia were made (20 μm thick) using the frozen section technique (Microtome SM2010, Leica). Obtained brain sections were washed with PBS, PBST (0.5% Triton X-100), and blocked with PBST containing 10% normal goat serum (NGS) and 2% bovine serum albumin (BSA). After blocking, brain sections were incubated with anti-tyrosine hydroxylase antibody (rabbit polyclonal, 1:1000, ab112), anti-tyrosine hydroxylase antibody (chicken polyclonal, 1:1000, ab76442), anti-dopamine transporter antibody (rat monoclonal, 1:500, ab5990), anti-vmat2 antibody (rabbit polyclonal, 1:1000, VMAT2-Rb-Af720), anti-gephyrin antibody (mouse monoclonal, 1:500, 147 111), anti-RFP antibody (mouse monoclonal, 1:1000, MA5-15257), anti-GFP antibody (chicken polyclonal, 1:1000, GFP-1010), anti-bassoon antibody (guinea pig polyclonal, 1:500, 147 004), anti-bassoon antibody (mouse monoclonal, 1:500, ADI-VAM-PS003-D), anti-neuroligin 2 antibody (guinea pig polyclonal, 1:1000, Nlgn2-GP-Af760), anti-vgat antibody (rabbit polyclonal, 1:500, 131 003), anti-synaptotagmin 1 antibody (mouse monoclonal, 1:500, 105 011), anti-synaptotagmin 7 antibody (rabbit polyclonal, 1:200, 105 173), anti-synaptotagmin 5/9 antibody (rabbit polyclonal, 1:500, 105 053), anti-ALDH1a1 (rabbit polyclonal, 1:1000, HPA002123), anti-VGLUT2 antibody (rabbit polyclonal, 1:500, 135 403), anti-PSD95 antibody (mouse monoclonal, 1:500, MAB1596), anti-$GABA_AR\alpha1$ antibody (rabbit polyclonal, 1:1000, GABAARa1-Rb-Af660) in blocking solution at 4°C overnight, followed by secondary antibodies (goat anti-rabbit, goat anti-rat, goat anti-mouse, goat anti-chicken, goat anti-guinea pig, Invitrogen, 1:1000) conjugated to Alexa 405, Alexa 488, Alexa 594, and Alexa 647 fluorophores in blocking solution at room temperature for 2 h. After washing with PBST and PBS, brain slices were mounted to slides using mounting medium (P36934 or P36935, Invitrogen).

For quantitative analysis, images were captured by FV1000 confocal laser scanning microscope (Olympus) using a 60x/1.35 NA oil immersion objective (image size: 512× 512 pixels), LSM780N multi-photon confocal laser scanning microscope with airyscan (Carl Zeiss) using a 63x/1.46 NA oil immersion objective (zoom factor: 3, image size: 912 × 912 pixels), and LSM880 multi-photon confocal laser scanning microscope with airyscan (Carl Zeiss) using a 63x/1.4 NA oil immersion objective (zoom factor: 3, image size: 6972 × 6972 pixels for stitched images or 1248 × 1248 pixels) and a 40x/1.2 NA water immersion objective (zoom factor: 3,

image size: 1248 × 1248 pixels). Imaging areas were randomly selected and then images were captured from each target brain region. Acquired images were further analyzed by Zen software (Carl Zeiss), ImageJ program (NIH, measure function), and MATLAB (MathWorks, custom codes). For dendritic synapse clustering analysis, the whole dendrite was divided into two compartments (proximal and distal). The half of the dendritic compartment close to the soma was analyzed as a proximal dendrite and the other half of the dendrite away from the soma was considered a distal dendrite.

### Expansion microscopy

For expansion microscopy, we referred to the expansion microscopy methods.[17] The expansion factor was measured as a 5-fold linear expansion. Images were captured by LSM980 multi-photon confocal laser scanning microscope (Carl Zeiss) using a 40x/1.2 NA water immersion objective (image size: 4895× 4895 pixels with 2 × 2 stitching). Acquired images were further analyzed by Zen software (Carl Zeiss), ImageJ program (NIH, measure function), and MATLAB (MathWorks, custom codes).

### dLight dopamine imaging

For dLight dopamine imaging, we referred to the evoked $GRAB_{DA}$ imaging methods.[55] Fluorescence imaging was performed using an Olympus BX51WI epifluorescence microscope. Fluorescent signals were excited by a 470 nm LED (Thor labs, SOLIS-470C), collected through a 4× objective, and digitized with a scientific complementary metal-oxide-semiconductor camera (Hamamatsu, Orca-Flash4.0 V3). Evoked responses were acquired at 512 × 512 pixels/frame, 40 frames/s, with an exposure time of 10 ms. Each pixel represents a physical area of 3.3 × 3.3 $\mu m^2$.

### Brain slice preparation for electrophysiology

Coronal brain slices containing striatal regions (DLS, DMS, NAc core, NAc shell, OT), cortex (ACC, M1), and extrastriatal basal ganglia (GPe, GPi, STN) were obtained (300 μm thick) for whole-cell patch clamp recording and FSCV.[54] Mice were anesthetized with isoflurane (Piramal Critical Care), decapitated, and the brain was taken out, briefly exposed to ice-chilled artificial cerebrospinal fluid (ACSF) containing 125 mM NaCl, 2.5 mM KCl, 1.25 mM $NaH_2PO_4$, 25 mM $NaHCO_3$, 1 mM $MgCl_2$, 2mM $CaCl_2$ and 15 mM glucose oxygenated with 95% $O_2$ and 5% $CO_2$. Acute brain slices were prepared using a tissue vibratome (Leica, VT 1200S) in ice-cold ACSF. Brain slices were first maintained in ACSF for 30 min at 34°C and then another 30 min at room temperature. After recovery, slices were transferred to a submerged recording chamber perfused with ACSF at a rate of 2–3 mL/min at 30°C–31°C. Brain slices were used for electrophysiological recording within 4 h after recovery.

### Electrophysiology, optogenetic stimulation, and pharmacology

Neurons in striatal regions, cortex, and extrastriatal basal ganglia were visually identified by conventional IR-DIC optics (BX51WI, Olympus).[54] Whole-cell voltage-clamp recordings were made with borosilicate glass pipettes (2.5–3.5 MΩ) filled with $Cs^+$ based low $Cl^-$ internal solution containing 135 mM $CsMeSO_3$, 10 mM HEPES, 1 mM EGTA, 3.3 mM QX-314, 0.1 mM $CaCl_2$, 4 mM Mg-ATP, 0.3 mM $Na_3$-GTP, 8 mM $Na_2$-phosphocreatine (290–300 mOsm, pH 7.3 with CsOH). To measure inhibitory and excitatory synaptic currents from the same neuron, membrane potential was first held at +0 mV (reversal potential of ionotropic glutamate receptors) to measure inhibitory synaptic currents and then continuously held at −70 mV (reversal potential of chloride) to measure excitatory synaptic currents under the voltage clamp mode (liquid junction potential corrected). Access resistance was 10–20 MΩ and only cells with a change in access resistance <20% were included in the analysis. Whole-cell patch clamp recordings were performed using Multiclamp 700B (Molecular Devices) and signals were filtered at 2 kHz and digitized at 10 kHz (NI PCIe-6259, National Instruments). Recording data were monitored and acquired by WinWCP (Strathclyde software, http://spider.science.strath.ac.uk/sipbs/software_ses.htm), further analyzed offline using Clampfit 10.7 software (Molecular Devices) and OriginPro 2017 (OriginLab). To stimulate ChR2-expressing dopaminergic or intra-striatal collateral axons, blue laser light (450 nm, 1 msec pulses with 60 s intervals, 50% of saturation power under the objective less than 10 mW) from a diode laser (MDL-III-450, Opto Engine LLC) was focused on the back focal plane of the objective to generate wide-field illumination. GABA and glutamate co-transmission from DA axon terminals were recorded from striatal regions (DLS, DMS, NAc core, NAc shell, OT), cortex (ACC, M1), and extrastriatal basal ganglia (GPe, GPi, STN) by optogenetically activating DA terminals. For the experiments demonstrating the oIPSCs and oEPSCs in our data are exclusively mediated by $GABA_A$ and glutamate receptors, we bath-applied $GABA_A$ receptor antagonist (Gabazine, Tocris, #1262) or glutamate receptors antagonists (CNQX + D-AP5, Tocris, #0190, #0106) during the recording session.

To test the physiological effects of acute inhibition of calcium channels on GABAergic transmission from DA and GABAergic neurons, we used selective T-type calcium channel blocker (NNC 55–0396, 1 μM, alomone labs, N-205), N-type calcium channel blocker (ω-conotoxin, 100 nM, alomone labs, C-300), P/Q-type calcium channel blocker (ω-agatoxin, 200 nM, alomone labs, STA-500) and these blockers were bath-applied during the recording session. For the experiment measuring strontium-induced asynchronous GABA release from DA and GABAergic terminals, another ASCF which contained strontium chloride hexahydrate (4 mM, Sigma-Aldrich, Cat. No. 255521) in place of calcium was made and after recording oIPSC with normal ACSF, this calcium-containing ACSF was replaced by strontium-containing ACSF. Asynchronous GABA release at DA and GABAergic (iSPN to dSPN) synapses were recorded from SPNs in DLS by optogenetically activating DA and GABAergic axon terminals. The amplitude and frequency of strontium-induced asynchronous IPSC were analyzed by using Mini Analysis software (Synaptosoft). To measure strontium-induced asynchronous GABA release using high chloride internal solution, we used a $Cs^+$ based high $Cl^-$ internal solution containing

126 mM CsCl, 8 mM NaCl, 10 mM HEPES, 0.2 mM $MgCl_2$, 2 mM QX-314, 1 mM EGTA, 0.1 mM $CaCl_2$, 4 mM Mg-ATP, 0.3 mM $Na_3$-GTP, 8 mM $Na_2$-phosphocreatine (290–300 mOsm, pH 7.3 with CsOH). We used glutamate receptors antagonists (CNQX + D-AP5, Tocris, #0190, #0106) to block glutamatergic currents and held the membrane potential at −70 mV. To measure strontium-induced asynchronous GABA release with the inhibition of nearby neurons with DREADDs, 5 μM Clozapine N-oxide dihydrochloride (Tocris, #6329) was bath-applied during the recording session. To measure the paired pulse ratio (PPR) of GABA transmission at DA synapses in the dorsal striatum, we optogenetically stimulated DA terminals by using a paired light stimulus (100 ms interval). The calcium concentration of ACSF was reduced to 1 mM in order to easily visualize the second oIPSC peak. To maintain the concentration of divalent cations in ACSF, the magnesium concentration was increased to 2 mM. To measure the PPR of GABA transmission at DA synapses in the dorsal striatum using weak stimulation, we optogenetically stimulated DA terminals by using a paired light stimulus (100 ms interval). We used glutamate receptors antagonists (CNQX + D-AP5, Tocris, #0190, #0106) to block glutamatergic currents and held the membrane potential at −30 mV. We also reduced the optogenetic stimulation to 10% of saturation power under the objective less than 10 mW with a 6% ND filter (U-25ND6, Olympus). To measure the PPR of GABA transmission at DA synapses in the dorsal striatum using ChETA, we optogenetically stimulated DA terminals by using a paired light stimulus (100 ms interval). All PPR experiments were carried out under normal ACSF conditions unless otherwise noted. To simultaneously measure DA transmission and GABA co-transmission in a single SPN, we used a $K^+$ based high $Cl^-$ internal solution containing 66 mM $KMeSO_3$, 70 mM KCl, 10 mM HEPES, 1 mM EGTA, 0.1 mM $CaCl_2$, 4 mM Mg-ATP, 0.3 mM $Na_3$-GTP, 8 mM $Na_2$-phosphocreatine (290–300 mOsm, pH 7.3 with KOH). We used glutamate receptors antagonists (CNQX + D-AP5, Tocris, #0190, #0106) to block glutamatergic currents and held the membrane potential at −60 mV.

### Fast-scanning cyclic voltammetry (FSCV)

Extracellular DA release was recorded by FSCV using carbon-fiber microelectrodes (7 μm diameter carbon fiber sealed by glass, 50–100 μm exposed tip length beyond the tapered glass seal) from striatal regions (DLS, DMS, NAc core, NAc shell, OT), cortex (ACC, M1), and extrastriatal basal ganglia (GPe, GPi, STN).[54] To detect DA release, a triangular scanning waveform was applied to the carbon fiber electrode from −0.4 V (vs. AgCl reference electrode) to +1.3 V and back (8.5 msec waveform width) at a scan rate of 400 V/s (repeated at 10 Hz). The carbon fiber electrode was held at −0.4 V between scans. Cyclic voltammograms were background-subtracted by averaging 10 background scans. To evoke DA release from DA synapses, ChR2-expressing DA axon terminals were stimulated by blue laser light (450 nm, 2 ms pulse width). Oxidation current by optogenetically evoked DA release was detected and monitored using the TarHeel CV system. Changes in dopamine concentration were quantified by plotting the peak oxidation current of the voltammogram over time. The carbon fiber electrode was calibrated at the end of each experiment to convert oxidation current to DA concentration using DA (10 μM, Tocris, Cat. No. 3548) in ACSF.

### Virus purchase

AAV-hSyn-GFP (AV5075E, UNC), AAV-hSyn-DIO-mCherry (50459-AAV5, Addgene), AAV-Ef1a-DIO ChETA-EYFP (26968-AAV5, Addgene), AAV-hSyn-hM4D(Gi)-mCherry (50475-AAV5), AAV-*syn*-dLight1.3b (135762-AAV9, Addgene), AAV9.hSyn.tdTomato.T2A.m.GIRK2-1-A22A.WPRE.bGH (V8414S, Upenn) were purchased from UNC vector core, Addgene, and Upenn, respectively. The production titer was $5.6 \times 10^{12}$ viral genomes/ml for AAV-hSyn-GFP, $7 \times 10^{12}$ viral genomes/ml for AAV-hSyn-DIO-mCherry, $2 \times 10^{13}$ viral genomes/ml for AAV-Ef1a-DIO ChETA-EYFP, $7 \times 10^{12}$ viral genomes/ml for AAV-hSyn-hM4D(Gi)-mCherry, $2.4 \times 10^{13}$ viral genomes/ml for AAV-*syn*-dLight1.3b, and $5.37 \times 10^{13}$ viral genomes/ml for AAV9.hSyn.tdTomato.T2A.m.GIRK2-1-A22A.WPRE.bGH.

### shRNA expression and verification of shRNA-mediated knockdown of NLGN2 (NL2)

NLGN2-specific and control shRNAs were expressed in the pSicoR vector (#21907, Addgene).[56] We tested three different pSicoR vectors encoding NLGN2-specific shRNA expression cassettes for their ability to knockdown NLGN2 expression in HEK293T (ATCC CRL3216) cells; the pSicoR-control served as a nontarget control shRNA containing nonhuman or mouse shRNA (50′-TCGCATAGCGTATGCCGTT-3′). Three kinds of shRNA were synthesized by the following method: Two kinds of oligos were purchased (Sequence of oligos; [phos]5′-t [sense sequence of target] ttcaagaga [reverse complement sequence of target] ttttttc-3′ and [phos]5′-tcgagaaaaaa [sense sequence of target] tctcttgaa [reverse complement sequence of target] a-3′). The sequence information of the three candidates for the shRNA is as follows: mNlgn2-sh1: 5′-CAATCCGCCAGACACAGATAT-3′, mNlgn2-sh2: 5′-TCTGC CACCTGAGTCTGATAT-3′, mNlgn2-sh3: 5′-GACCCTGAACGCATCACTATC-3′. The two oligos were annealed with annealing buffer (in mM; 200 potassium acetate, 60 HEPES-KOH, 4 Mg-acetate, pH 7.3 was adjusted by KOH) and incubated at 95°C for 5 min and 70°C for 10 min. The annealed double-stranded oligo was inserted into HpaI-XhoI restriction enzyme sites within the pSicoR vector and verified by sequencing.

### α-synuclein-expressing AAV generation

We used a pHM6-α-synuclein-A53T (Addgene #40825) construct to generate AAV-α-synuclein-A53T and AAV-α-synuclein-A53T-mediated mouse model of Parkinson's disease.[54] The α-synuclein-A53T cDNA was generated into BamHI/XhoI restriction enzyme sites of AAV-MCS (multi cloning site) expression vector (Cell Biolabs Inc., Cat. No. VPK-410) by in-Fusion cloning scheme.[57] This vector was created by expression under cytomegalovirus (CMV) immediate-early enhancer and promoter. This plasmid construct

was verified by nucleotide sequencing. This viral vector was pseudo-typed where the transgene was flanked by inverted terminal repeats of AAV2 packaged in an AAV-DJ capsid. AAV-DJ was engineered using a DNA family shuffling technology to create a hybrid capsid from eight AAV serotypes. Additionally, AAV-DJ-CMV-α-synuclein (A53T) vector was purified by iodixanol gradient ultracentrifugation by the Korea Institute of Science and Technology (KIST) Virus Facility. The production titer was $2.8 \times 10^{13}$ viral genomes/ml for AAV-DJ-CMV-α-synuclein (A53T).

### Quantitative real-time PCR

Gene silencing assays using shRNAs targeting NLGN2 candidates were tested by quantitative real-time PCR (qRT-PCR). All shRNAs were transfected into HEK293T cells. Approximately 24 h after transfection, total RNA was isolated from HEK293T cells using an RNA extraction kit (Intro, #17221) according to the manufacturer's instructions. Complementary DNA (cDNA) was synthesized from 1 μg total RNA, and reverse transcription was performed using a SuperScript cDNA synthesis kit (Bioneer, AccuPower CycleScript RT PreMix & Master Mix (K-2044)) according to the manufacturer's instructions. qRT-PCR was performed using an SYBR Green expression assay (Thermo Fisher Scientific, Power SYBR Green Master Mix (4367659)). Primer sets for NLGN2 were purchased from Macrogen; mNlgn2-qRT-F: TTCCCACCACTCAGAAGGAC, mNlgn2-qRT-R: GTGCTGTCTTCTCGGTCACA. GAPDH was used as a housekeeping gene. The delta-delta Ct method was used to calculate fold changes in gene expression.[58] Among the 3 shRNA candidates, mNlgn2-sh1 was the most effective to knockdown NLGN2 and was chosen for AAV production.

### AAV cloning and production

For adeno-associated-virus (AAV)-based shRNA expression, pSicoR-shRNA vectors with XbaI/HindIII-containing enzymatic site were inserted into the pAAV-minCMV-mCherry (#27970, Addgene) vector by the same enzymatic site. The CMV promoter in these vectors was replaced with the hSyn promoter by infusion cloning (Clontech, In-Fusion HD Cloning Kit). AAV-U6-scrambled RNA-hSyn-mCherry and AAV-U6-mNLGN2-shRNA-hSyn-mCherry were thereafter purified by iodixanol gradient ultracentrifugation by the KIST Virus Facility. The production titer was $6.56 \times 10^{13}$ viral genomes/ml for AAV-U6-scrambled RNA-hSyn-mCherry and $3.9 \times 10^{13}$ viral genomes/ml for AAV-U6-mNLGN2-shRNA-hSyn-mCherry.

### Stereotaxic viral injection for sparse labeling

Stereotaxic virus injection was conducted on over 8–10 weeks old male and female mice (DAT-Cre, A2A-Cre) and performed using a stereotaxic system (51730, Stoelting).[54] Before surgery, mice were deeply anesthetized by intraperitoneal injection of zoletil (60 mg/kg, Virbac Korea) and rompun (15 mg/kg, Bayer Korea) mixture solution (zoletil: rompun: saline = 4 : 1: 20). A total volume of 300 nL virus solution (1:50 dilution of AAV-hSyn-GFP for DAT-Cre, 1:50 dilution of AAV-hSyn-GFP mixed with 1:2 dilution of AAV-hSyn-DIO-mCherry for A2A-Cre) was injected into DLS (coordinates used, AP: +1.3 mm, ML: ±2.25 mm from bregma, DV: −2.2 mm from exposed dura mater) to achieve sparse labeling of neurons. A glass micropipette with a long narrow tip (size: 10–20 μm) was made using a micropipette puller (P-1000, Sutter Instrument) to deliver the virus. The glass pipette was slowly reached to the target area and left for 5 min before virus injection. Virus solution (300 nL) was injected at an infusion rate of 100 nL/min and withdrawn 10 min after the end of the injection. After injection, the scalp was sutured and mice were returned to their home cages. Virus-injected mice were used for immunohistochemistry experiments 3 weeks after injection.

### Stereotaxic viral injection for NLGN2 (NL2) knockdown

Stereotaxic virus injection was conducted on over 6–10 weeks old male and female mice (DAT-Cre, DAT-Cre; Ai32, A2A-Cre; Ai32) and performed using a stereotaxic system (51730, Stoelting). Before surgery, mice were deeply anesthetized by intraperitoneal injection of zoletil (60 mg/kg, Virbac Korea) and rompun (15 mg/kg, Bayer Korea) mixture solution (zoletil: rompun: saline = 4 : 1: 20). A total volume of 1 μL virus solution (AAV-U6-scrambled RNA-hSyn-mCherry for control, AAV-U6-mNLGN2-shRNA-hSyn-mCherry for NL2 KD) was injected bilaterally into DLS (coordinates used, AP: +1.3 mm, ML: ±2.25 mm from bregma, DV: −2.2 mm from exposed dura mater). A glass micropipette with a long narrow tip (size: 10–20 μm) was made using a micropipette puller (P-1000, Sutter Instrument) to deliver the virus. The glass pipette was slowly lowered to the target area and left for 5 min before virus injection. Virus solution was injected at an infusion rate of 100 nL/min and withdrawn 10 min after the end of injection. After injection, the scalp was sutured and mice were returned to their home cages. Virus-injected mice were used for electrophysiology and immunohistochemistry experiments 6, and 12 weeks after injection. For the PPR experiment with the ChETA virus, an additional injection was conducted 2 weeks after the NL2 KD virus injection. A total volume of 1 μL ChETA virus solution (AAV5-Ef1a-DIO ChETA-EYFP) was injected bilaterally into the SNc (coordinates used, AP: −3.1 mm, ML: +1.2 mm from bregma, DV: −4.0 mm from exposed dura mater). Other conditions were similar to the previous injections. For DA transmission and GABA co-transmission measurements using the mGIRK2 virus, an additional injection was conducted 2 weeks after the NL2 KD virus injection. A total volume of 1 μL mGIRK2 virus solution (AAV9.hSyn.tdTomato.T2A.m.GirK2-1-A22A.WPRE.bGH) was injected bilaterally into the DLS (coordinates used, AP: +1.3 mm, ML: ±2.25 mm from bregma, DV: −2.2 mm from exposed dura mater). Other conditions were similar to the previous injections.

### Stereotaxic 6-OHDA injection

Stereotaxic 6-OHDA injection was conducted on over 8–14 weeks old male and female mice (DAT-Cre, DAT-Cre; Ai32) and performed using a stereotaxic system (51730, Stoelting). Before surgery, mice were deeply anesthetized by intraperitoneal injection

of zoletil (60 mg/kg, Virbac Korea) and rompun (15 mg/kg, Bayer Korea) mixture solution (zoletil: rompun: saline = 4 : 1: 20). A total volume of 300 nL 6-OHDA solution (1.25 mg/mL, dissolved in 0.9% sterile saline with 0.02% ascorbic acid) was injected unilaterally into left MFB (coordinates used, AP: −1.2 mm, ML: +1.2 mm from bregma, DV: −4.75 mm from exposed dura mater). A glass micropipette with a long narrow tip (size: 10–20 μm) was made using a micropipette puller (P-1000, Sutter Instrument) to deliver 6-OHDA. The glass pipette was slowly reached to the target area and left for 5 min before the 6-OHDA injection. 6-OHDA solution was injected at an infusion rate of 100 nL/min and withdrawn 10 min after the end of the injection. After injection, the scalp was sutured and mice were returned to their home cages. 6-OHDA-injected mice were used for electrophysiology and immunohistochemistry experiments 1, 3, and 7 days after injection. For dLight dopamine imaging, the mice were injected with the dLight virus 4 weeks before the injection of 6-OHDA. A total volume of 1 μL dLight virus solution (AAV-*syn*-dLight1.3b) was injected bilaterally into the DLS (coordinates used, AP: +1.3 mm, ML: ±2.25 mm from bregma, DV: −2.2 mm from exposed dura mater). Other conditions were similar to the previous injections.

### Stereotaxic α-synuclein-expressing AAV injection

Stereotaxic α-synuclein virus (AAV) injection was conducted on over 6–10 weeks old male and female mice (DAT-Cre, DAT-Cre; Ai32) and performed using a stereotaxic system (51730, Stoelting). Before surgery, mice were deeply anesthetized by intraperitoneal injection of zoletil (60 mg/kg, Virbac Korea) and rompun (15 mg/kg, Bayer Korea) mixture solution (zoletil: rompun: saline = 4 : 1: 20). A total volume of 1 μL α-synuclein virus solution (AAV-DJ-CMV-α-synuclein A53T) was injected unilaterally into left SNc (coordinates used, AP: −3.1 mm, ML: +1.2 mm from bregma, DV: −4.0 mm from exposed dura mater). A glass micropipette with a long narrow tip (size: 10–20 μm) was made using a micropipette puller (P-1000, Sutter Instrument) to deliver the virus. The glass pipette was slowly reached to the target area and left for 5 min before virus injection. Virus solution was injected at an infusion rate of 100 nL/min and withdrawn 10 min after the end of the injection. After injection, the scalp was sutured and mice were returned to their home cages. Virus-injected mice were used for electrophysiology and immunohistochemistry experiments 1, 2, and 4 weeks after injection.

### Stereotaxic viral injection for DREADDs

Stereotaxic virus injection was conducted on over 8–12 weeks old male and female mice (DAT-Cre; Ai32) and performed using a stereotaxic system (51730, Stoelting). Before surgery, mice were deeply anesthetized by intraperitoneal injection of zoletil (60 mg/kg, Virbac Korea) and rompun (15 mg/kg, Bayer Korea) mixture solution (zoletil: rompun: saline = 4 : 1: 20). A total volume of 1 μL virus solution (AAV-hSyn-DIO-hM4D(Gi)-mCherry) was injected bilaterally into the DLS (coordinates used, AP: +1.3 mm, ML: ±2.25 mm from bregma, DV: −2.2 mm from exposed dura mater). A glass micropipette with a long narrow tip (size: 10–20 μm) was made using a micropipette puller (P-1000, Sutter Instrument) to deliver the virus. The glass pipette was slowly lowered to the target area and left for 5 min before virus injection. Virus solution was injected at an infusion rate of 100 nL/min and withdrawn 10 min after the end of the injection. After injection, the scalp was sutured and mice were returned to their home cages. Virus-injected mice were used for electrophysiology experiments 4 weeks after injection.

## QUANTIFICATION AND STATISTICAL ANALYSIS

### Spot detection and synapse extraction analysis (used for synapse analysis)

To extract synapses from the acquired image, we implemented a general method for spot detection.[59–61] The method exploits mathematical morphological processing based on set theory. By considering objects in the acquired images as sets, signal enhancement and spot detection can be accomplished exploiting combinations of logical operators in set theory. This method is divided into three parts: denoising, signal enhancement, and spot extraction. At the denoising step, the acquired images are processed by Gaussian filter with $\sigma = 0.5$. For signal enhancement, three combined thresholding algorithms with top-hat transform, hard thresholding, and Otsu thresholding are applied to the resulting images. Top-hat transform of an image $I(m)$ is represented as:

$$\mathrm{T}(I(m)) = I(m) - I(m) \circ s(m)$$

where $\circ$ denotes the opening operator in morphological processing and $s(m)$ denotes the structuring element. Our structuring element $s(m)$ for applying top-hat transform is circular shape with size of 10 X 10. Hard thresholding is expressed as:

$$\mathrm{H}(I(m)) = \begin{cases} I(m) & \text{if } I(m) > threshold \\ 0 & \text{if } I(m) < threshold \end{cases}$$

Threshold value of hard thresholding is 40000. After applying top-hat transform and hard thresholding to the acquired images, Otsu's thresholding method is exploited to the processed images to enhance the fluorescent signal from the actual object and suppress the background signal. From the signal-enhanced images, spots are extracted using combined morphological filters, consisting of two morphological operations: filling and opening. Filling is employed to fill out holes in fluorescent spots, and opening is performed to smooth the contour of spots and remove irrelevant fluorescent signals to the synaptic structure. The extracted spots are clustered within the set of images (presynaptic and postsynaptic) corresponding to the distance among the spots, which allows the images to delineate presynaptic structures (colocalization between TH and presynaptic marker Bassoon or VMAT2 in case of GABAergic-like DA synapses, colocalization between RFP and VGAT in case of conventional GABA synapses, and colocalization

between TH and VGlut2 in case of glutamatergic presynaptic sites on DA boutons) and postsynaptic structures (postsynaptic marker NL2 or gephyrin in case of GABAergic-like DA synapses, colocalization between GFP and NL2 in case of GABAergic-like DA synapses on a single dendrite or conventional GABA synapses on a single dendrite, colocalization between RFP and NL2 or gephyrin or $GABA_AR\alpha1$ in case of GABAergic-like DA synapses in NL2 control and KD virus injected mice, and colocalization between RFP and PSD95 in case of glutamatergic postsynaptic sites at DA synapses). By calculating the distance between presynaptic and postsynaptic clusters, the clusters with less than 0 pixel in distance were combined to constitute synapses. For shuffled NL2 analysis, we referred to the shuffling analysis methods and randomly shuffled NL2 signals to analyze the formation of GABAergic-like DA synapses.[5]

### dLight dopamine analysis

For the analysis of dLight signals, we referred to the evoked $GRAB_{DA}$ analysis methods.[55] For image analysis, regions of interest (ROIs) containing the striatum were manually selected in each image stack, and the backgrounds were estimated from the cortical regions where no sensor was expressed. For the quantification of evoked release, F0 was estimated as the average fluorescence signal over 0.5 s immediately before stimulation. $\Delta F/F0$ was then calculated for each pixel, and pixels with a $\Delta F/F0 > 0.1$ in response to electrical stimulation were considered as part of a release event.

### Point pattern analysis

The spatial analysis of GABAergic-like DA synapses was performed using Ripley's analysison both single group and group vs. group scale.[62,63] Ripley's function describes spatial characteristics of the sample (clustering or dispersion) over a range of distances. The edge corrected Ripley's function is defined as:

$$K(r) = \lambda^{-1}\sum_{i\neq j} k_{ij} I(d_{ij} \leq r) \Big/ N$$

where $\lambda$ is the density of a point pattern; $k_{ij}$ is the inverse of a portion of circumference with center at point $i$ and radius $r$, that lies within the boundary and passes through point $j$; function I is an indicator function; d is the Euclidean distance between points i and j; N is the number of points in the pattern. A variance stabilized version of the Ripley's K function was used in this study[64]:

$$H_r = \sqrt{\frac{K(r)}{\pi} - r}$$

Ripley's function was computed for each observed point pattern. Group vs. group analysis was also performed to establish whether point patterns from one group shared similar spatial characteristics with patterns from another (null) group. We assume that all m (the total number of generated patterns) patterns in the null group are generated by the same point process.

### Diggle-Cressie-Loosmore-Ford (DCLF) test

Diggle-Cressie-Loosmore-Ford (DCLF) test is based on the quantification of the difference between the H function of the observed pattern and the H function for the null group at the given spatial scale. We computed $H(r)$ for the test pattern $H_{obs}(r)$ and each pattern in the null group $H_i(r)$, then we estimated the summary function $\acute{H}(r)$ for the null group as follows:

$$\acute{H}(r) = \frac{1}{m+1}(H_1(r) + H_2(r) + \ldots + H_m(r) + H_{obs}(r))$$

Then, the maximum vertical separation between $H(r)$ and $\acute{H}(r)$ is:

$$T_{obs} = \int_0^R (H_{obs}(r) - \acute{H}(r))^2 dr$$

where R is maximum value of the interaction distance. To compute p value, the following formula can be used: $p = \frac{\sum_1^m I(T_{obs} > T_i)}{m+1}$, where $I(T_{obs} > T_i) = \begin{cases} 1, T_{obs} > T_i \\ 0, otherwise \end{cases}$ and $T_i$ is computed between the observed pattern and each pattern in the test group $(i = \overline{1,m})$.

### Statistics

All data were analyzed using Clampfit 10.7 (Molecular Devices), Mini Analysis (version 6.0.7, Synaptosoft), OriginPro 2017 (OriginLab), Zen software (version 2.5, Carl Zeiss), ImageJ (version 1.53c, NIH), and MATLAB (version R2017a, MathWorks). Statistical analysis was performed using GraphPad Prism software (version 10, GraphPad software). Summary statistics were all shown with box and whisker plot or mean ± SEM. Unpaired and paired student t-tests, one-way ANOVA with post-hoc Sidak's multiple comparison test, two-way repeated measures ANOVA with post-hoc Sidak's multiple comparison test, linear regression, Kolmogorov-Smirnov test were used to determine statistical differences (two-sided) between the groups. $p < 0.05$ was considered statistically significant. *$p < 0.05$, **$p < 0.01$, ***$p < 0.001$, ****$p < 0.0001$. Measured values and the details of statistical analysis were presented in Table S1.